Supporting Information

Elucidating the Copper–Hägg Iron Carbide Synergistic Interactions for Selective CO Hydrogenation to Higher Alcohols

Yongwu Lu,[†,⊗] Riguang Zhang,[‡,⊗] Baobao Cao,[§] Binghui Ge,[∥] Franklin (Feng) Tao,[⊥] Junjun Shan,[⊥] Luan Nguyen,[⊥] Zhenghong Bao,[†] Tianpin Wu,[#] Jonathan W. Pote,[†] Baojun Wang,[‡,*] and Fei Yu[†,*]

[†]Department of Agricultural and Biological Engineering, Mississippi State University, Mississippi State, MS 39762, United States

[‡]Key Laboratory of Coal Science and Technology of Ministry of Education and Shanxi Province, Taiyuan University of Technology, Taiyuan, Shanxi 030024, P.R. China

[§]School of Materials Science and Engineering, Southwest Jiaotong University, Chengdu, Sichuan 610031, P. R. China

[∥]Beijing National Laboratory for Condensed Matter Physics, Institute of Physics, Chinese Academy of Science, Beijing 100190, P.R. China

[⊥]Department of Chemical and Petroleum Engineering and Department of Chemistry, University of Kansas, Lawrence, KS 66045, United States

[#]X-ray Science Division, Advanced Photon Source, Argonne National Laboratory, Argonne, Illinois 60439, United States

* To whom correspondence should be addressed: Baojun Wang (wangbaojun@tyut.edu.cn); Fei Yu (fyu@abe.msstate.edu).

⊗Yongwu Lu and Riguang Zhang contributed equally to this work.

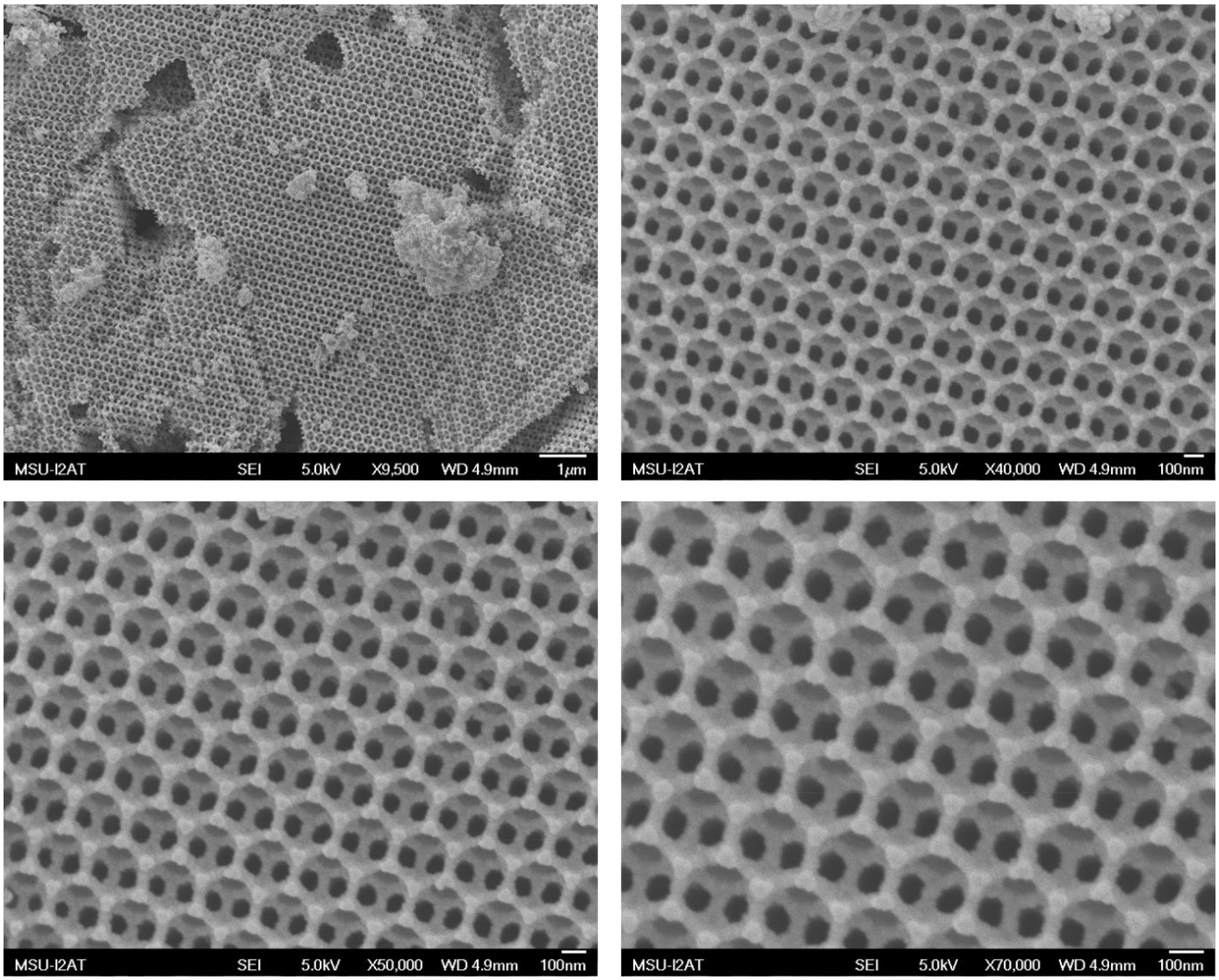

Figure S1. SEM images of 3DOM Cu_2Fe_1 catalyst under different magnifications.

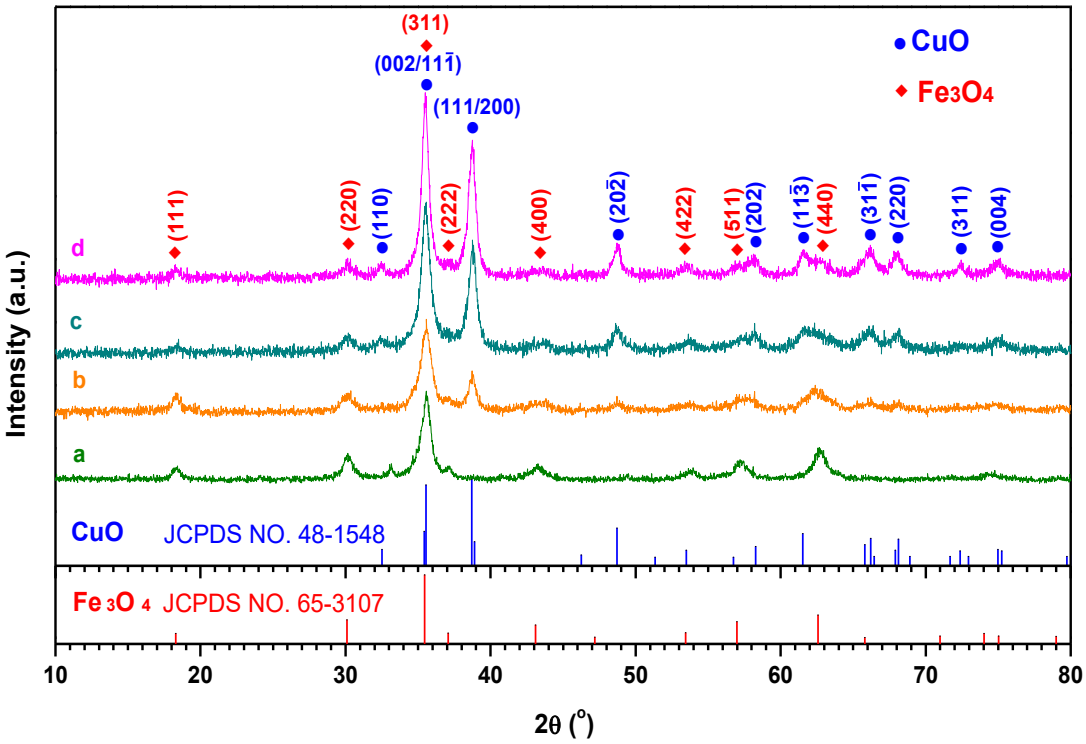

Figure S2. XRD pattern of fresh 3DOM Cu-Fe catalysts. (a) 3DOM Cu_1Fe_2, (b) 3DOM Cu_1Fe_1, (c) 3DOM Cu_2Fe_1, and (d) 3DOM Cu_3Fe_1.

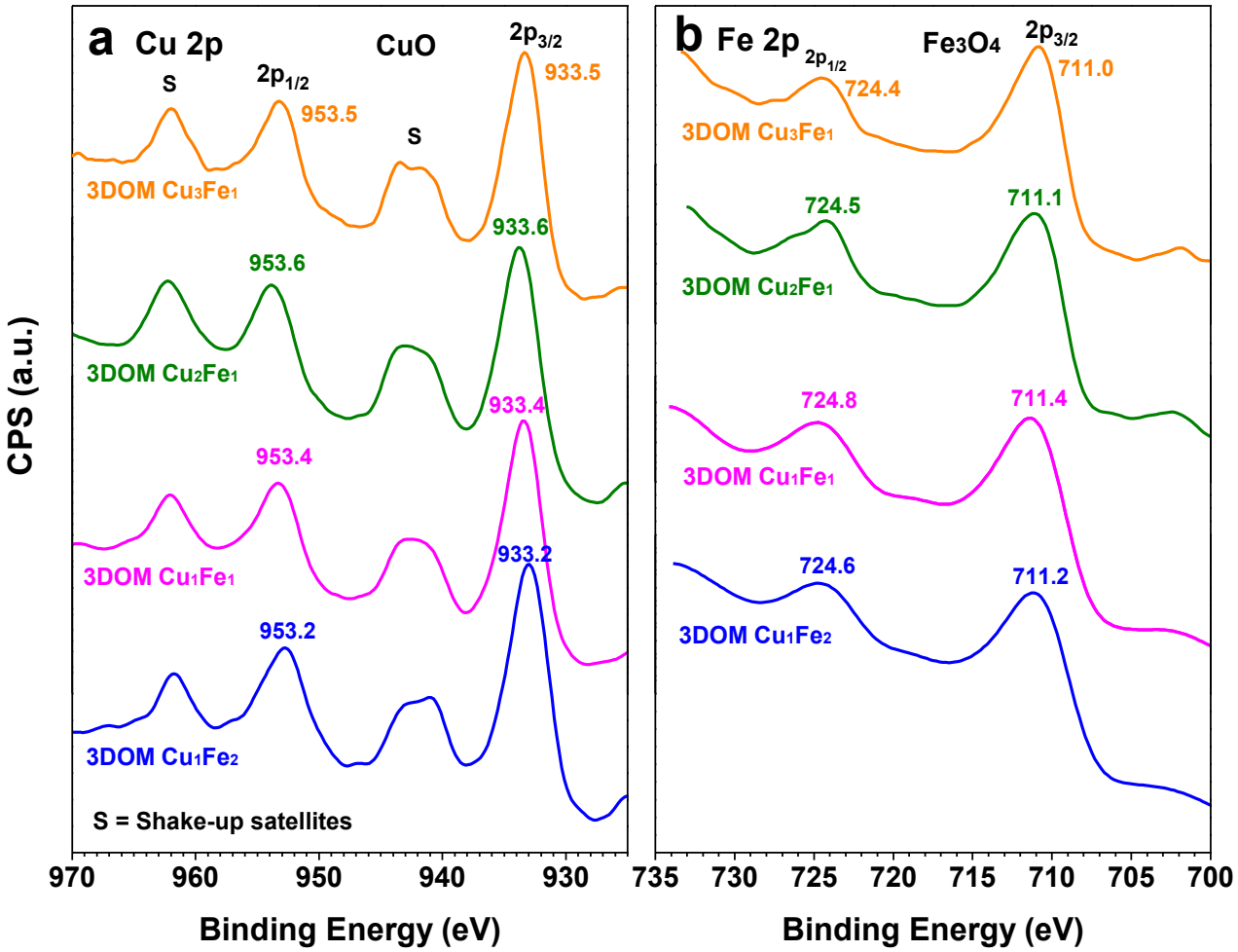

Figure S3. XPS spectra. (a) Cu 2p and (b) Fe 2p of fresh 3DOM Cu_1Fe_2, 3DOM Cu_1Fe_1, 3DOM Cu_2Fe_1, and 3DOM Cu_3Fe_1 catalysts.

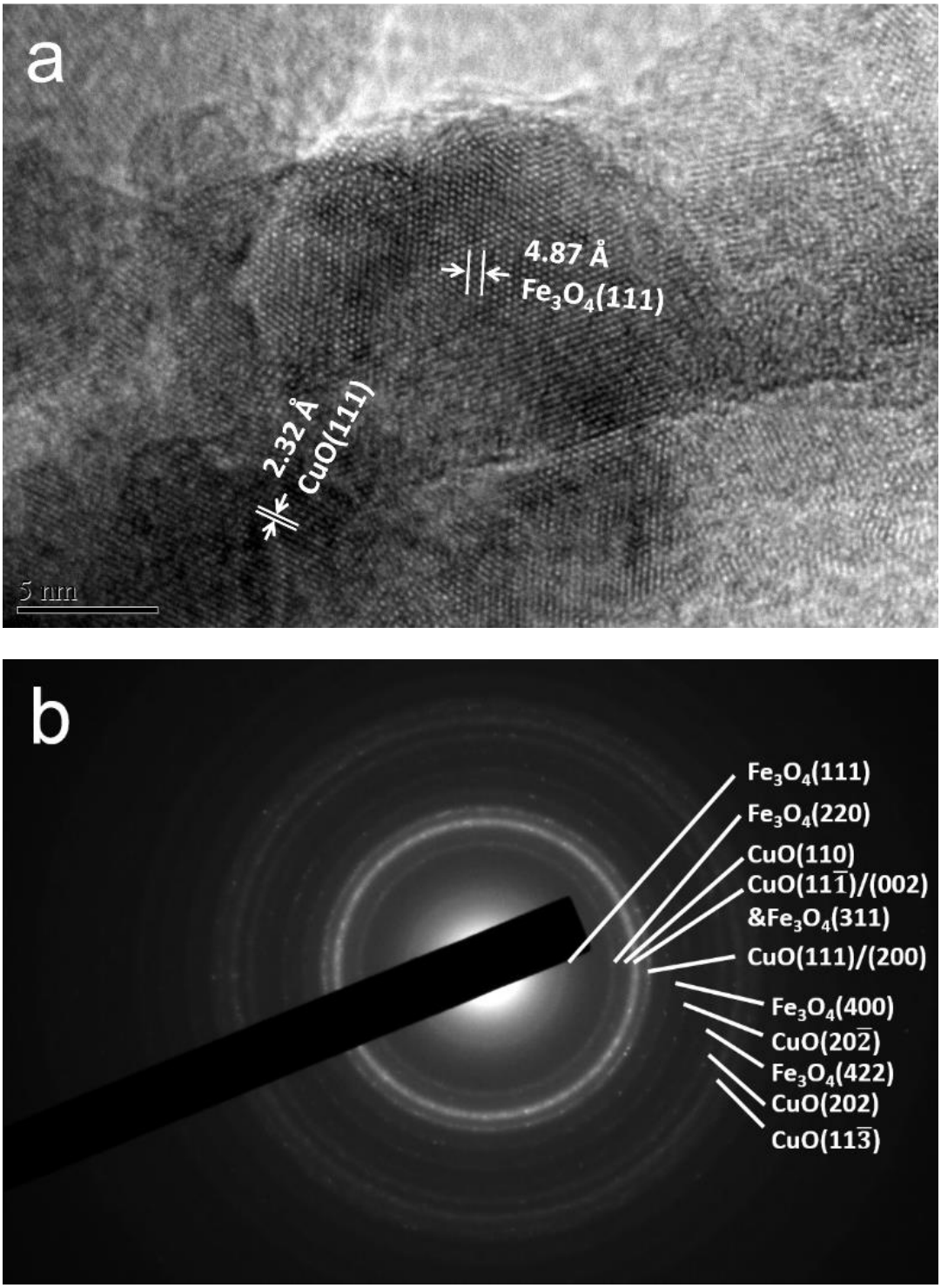

Figure S4. HRTEM image. (a) High-resolution TEM of fresh 3DOM Cu_2Fe_1 catalyst. (b) The corresponding indexed selected-area electron diffraction (SAED) pattern.

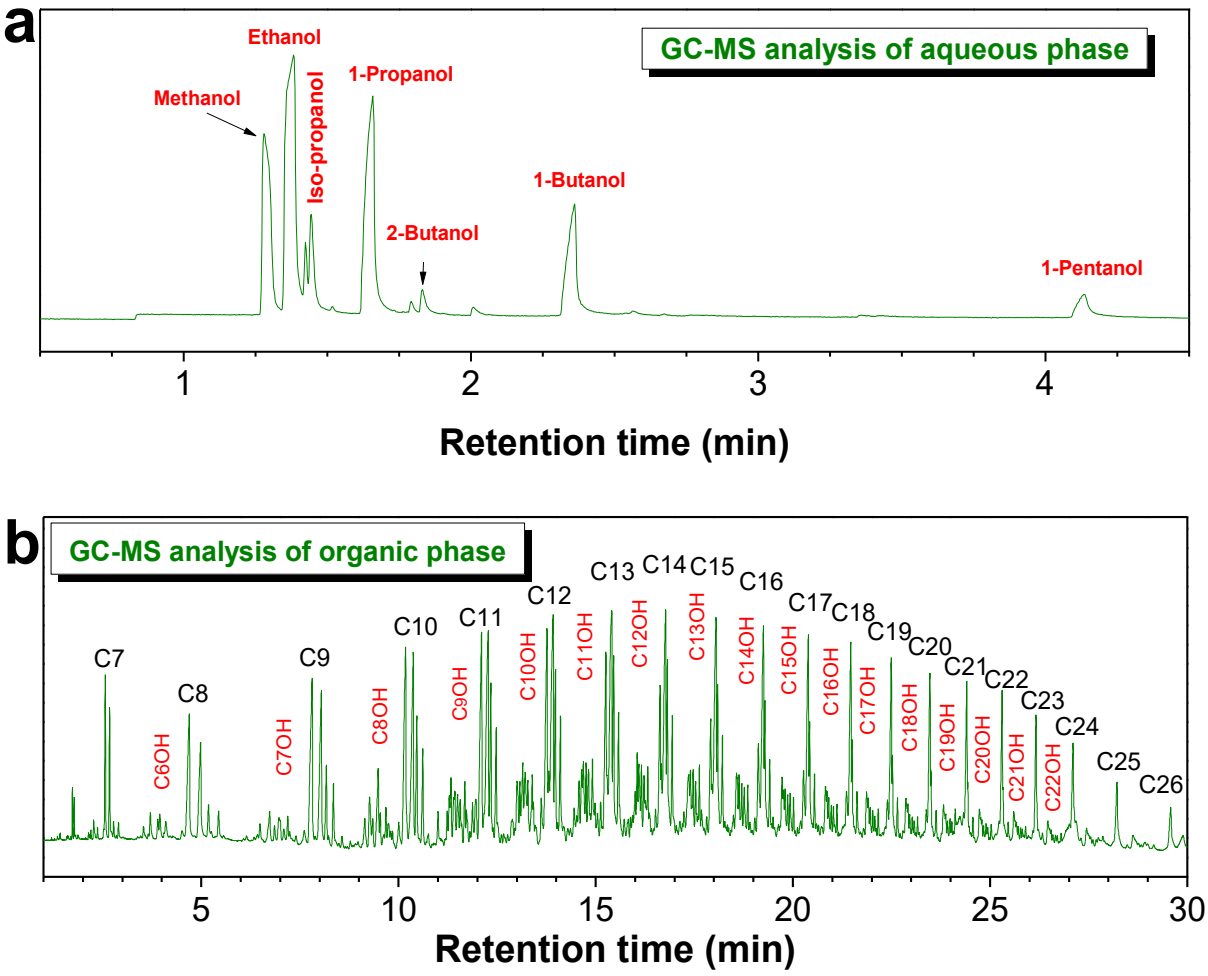

Figure S5. Gas chromatography-mass spectrometry (GC–MS) analysis of (a) aqueous and (b) liquid organic products from CO hydrogenation over 3DOM Cu_2Fe_1 catalyst. (Note: C_n, hydrocarbons; C_nOH, 1-alcohols).

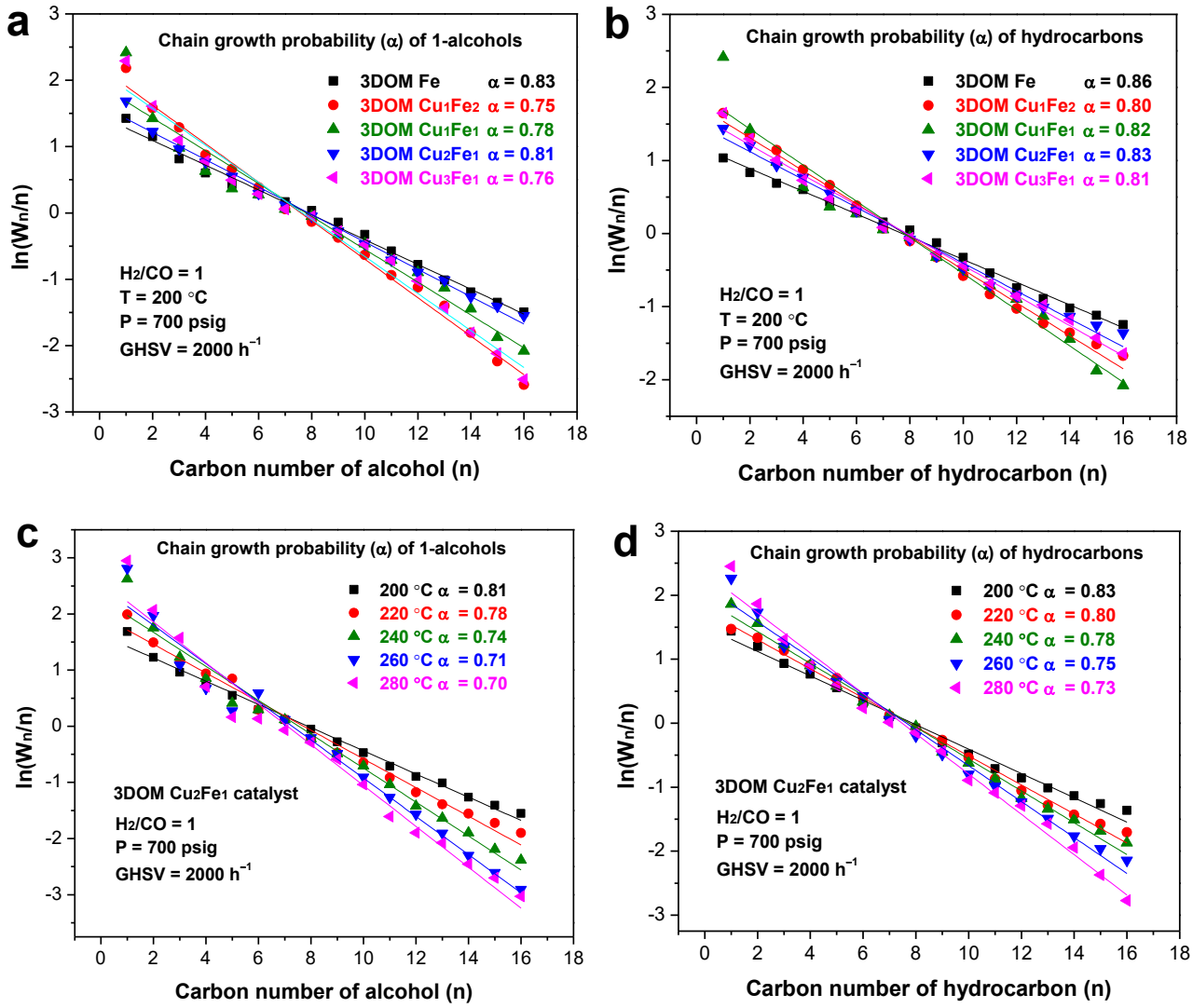

Figure S6. The Anderson–Schulz–Flory (ASF) plots. (a and b) The ASF plots for 1-alcohols and hydrocarbons distributions of 3DOM Cu-Fe catalysts, respectively. (Reaction conditions: P = 700 psig, T = 200 ℃, GHSV = 2000 h^{-1}, H_2/CO =1.0, time-on-stream of 120 h). (c and d) The ASF plots for 1-alcohols and hydrocarbons distributions of 3DOM Cu_2Fe_1 catalyst at different reaction temperatures (200–280℃), respectively. (Reaction conditions: P = 700 psig, GHSV = 2000 h^{-1}, H_2/CO =1.0, time-on-stream of 120 h). Note: The ASF chain growth probability α of products are calculated according to the equation of $\ln\left(\frac{W_n}{n}\right) = n\ln\alpha + \ln\frac{(1-\alpha)^2}{\alpha}$, where n is the number of carbon atoms in products, W_n is the weight fraction of products containing n carbon atoms, and $1-\alpha$ is the probability of chain termination.[1]

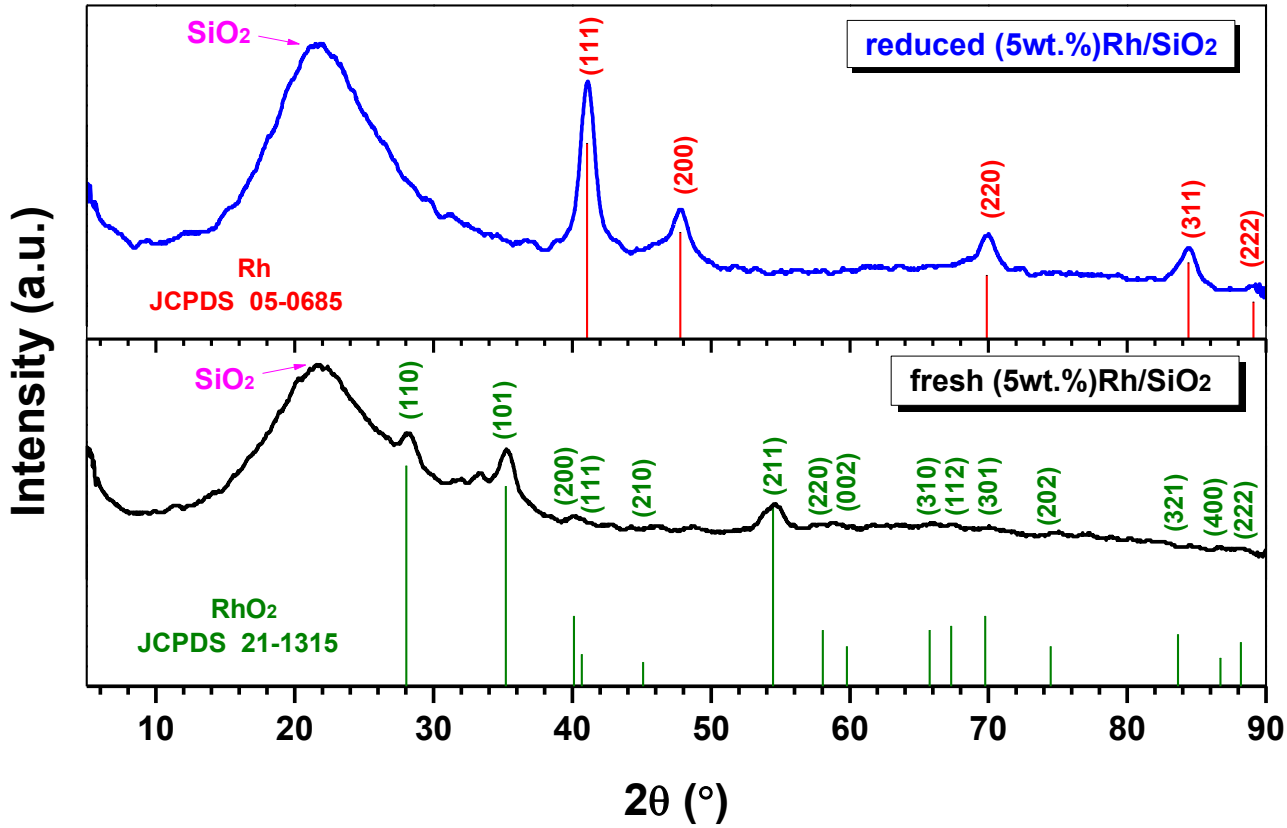

Figure S7. XRD patterns of fresh and reduced of (5wt.%)Rh/SiO_2 catalyst.

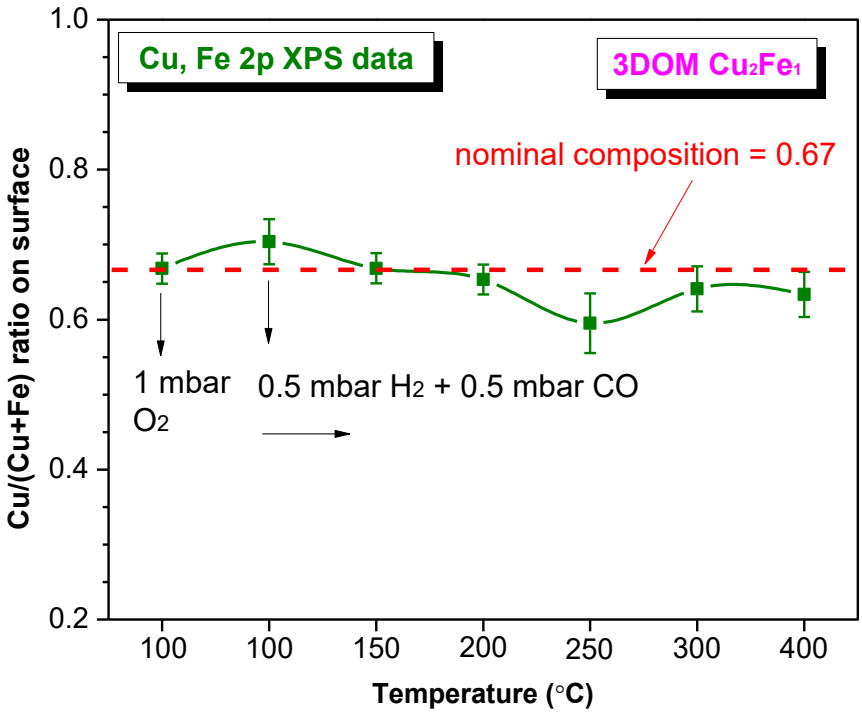

Figure S8. The evolution of Cu/(Cu+Fe) atomic ratio on surface of 3DOM Cu_2Fe_1 catalyst using *in situ* AP-XPS (with *in situ* O_2 pretreatment). The error of measurement of peak area is $\pm$5% of the corresponding peak area.

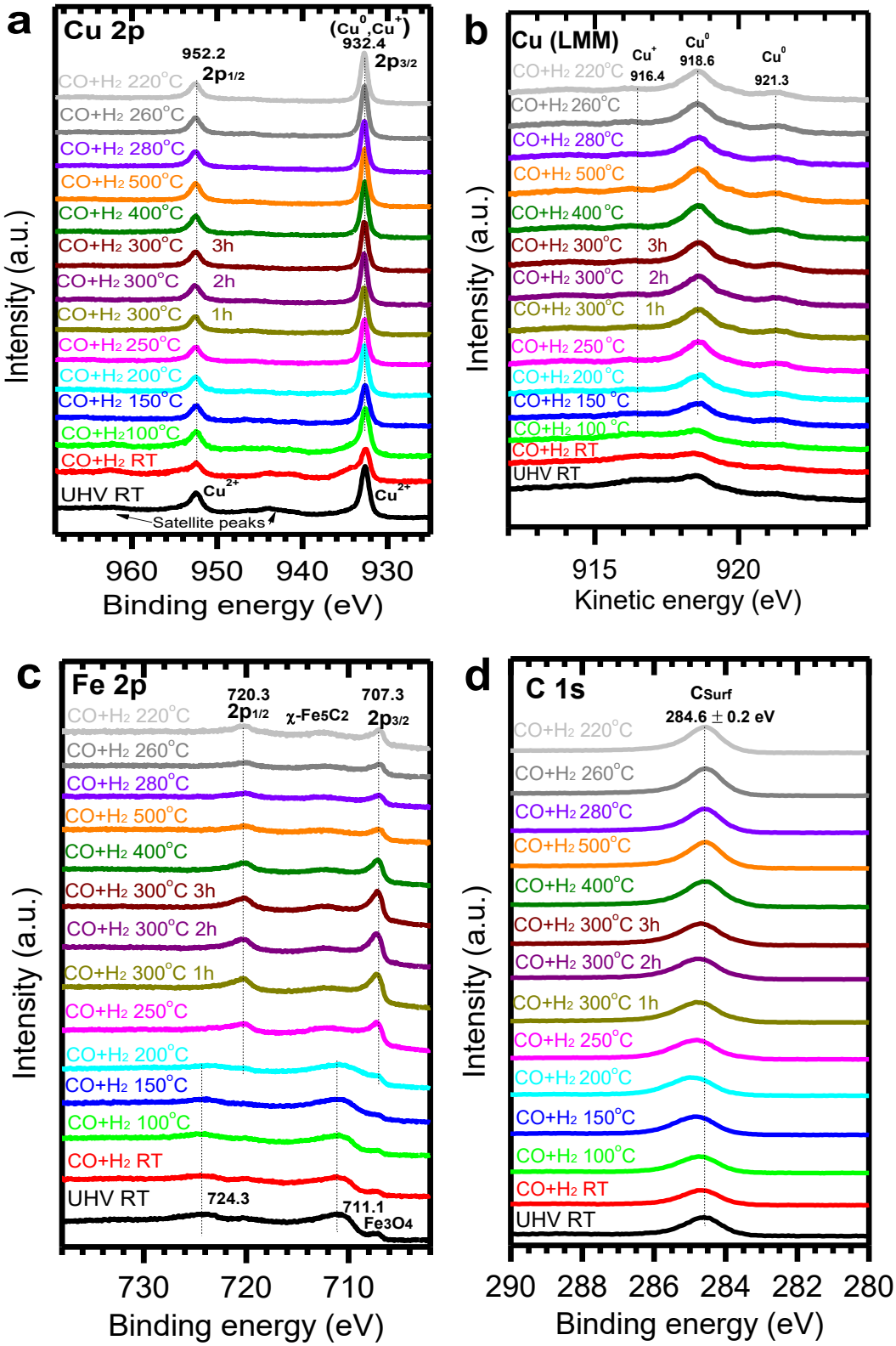

Figure S9. *In situ* studies of surface chemistry using AP-XPS for 3DOM Cu_2Fe_1 catalyst (without O_2 pretreatment) at different temperatures in H_2 and CO with a molar ratio of 1:1 at mbar pressure range. (a) Cu 2p, (b) Cu LMM, (c) Fe 2p and (d) C 1s.

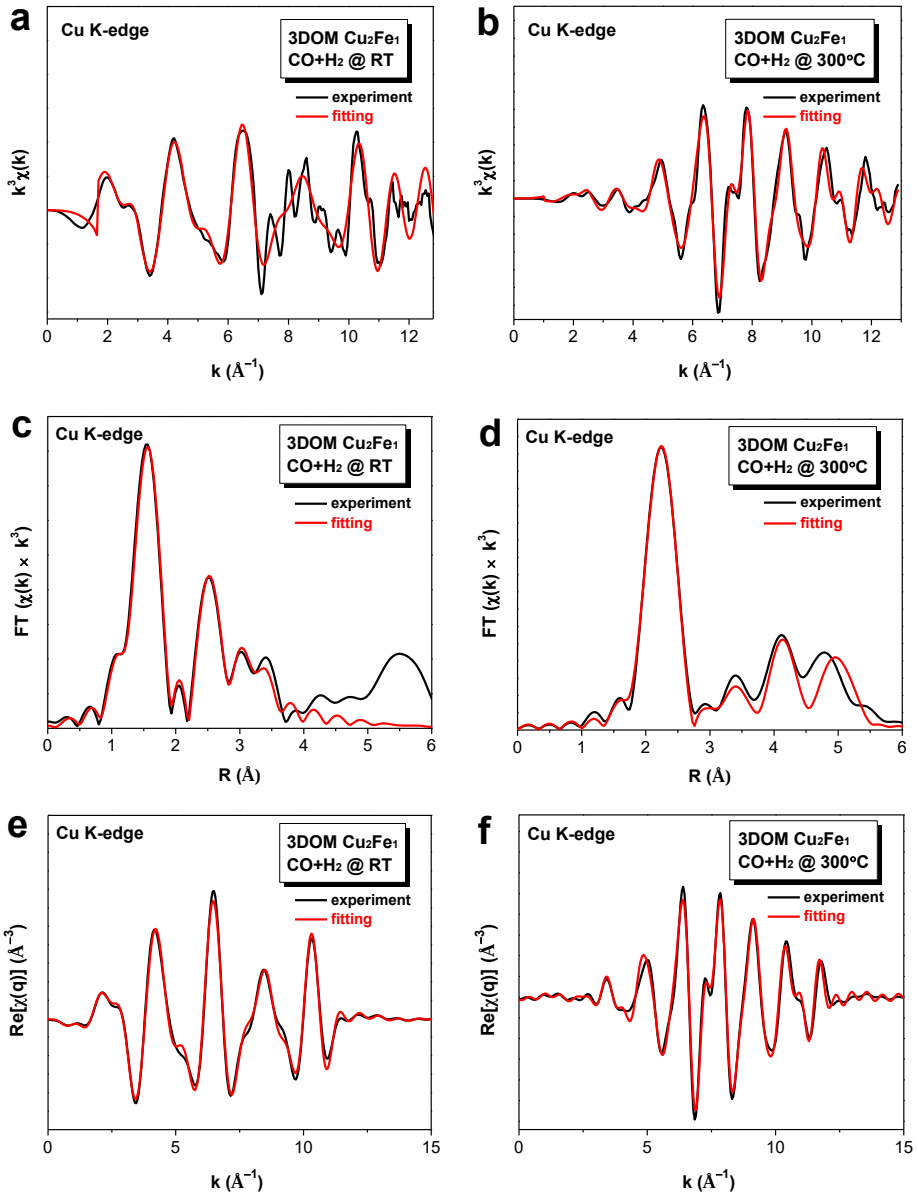

Figure S10. *In situ* $k^3\chi(k)$, Fourier transforms of [$k^3\chi(k)$] (R-space plot), and Re[χ(q)] (Å^{-3}) (q-space plot) spectra for the experimental Cu K-edge EXAFS signal of the 3DOM Cu_2Fe_1 catalyst at RT (a, c, e) and 300℃ (b, d, f) under CO+H_2 (H_2/CO = 1) gas and the fit (3DOM Cu_2Fe_1 CO+H_2@RT: Δk=2.0–11.0 Å^{-1} and ΔR=1.0–4.0 Å; 3DOM Cu_2Fe_1 CO+H_2@300℃: Δk=2.5–12.0 Å^{-1} and ΔR=1.7–5.1 Å).

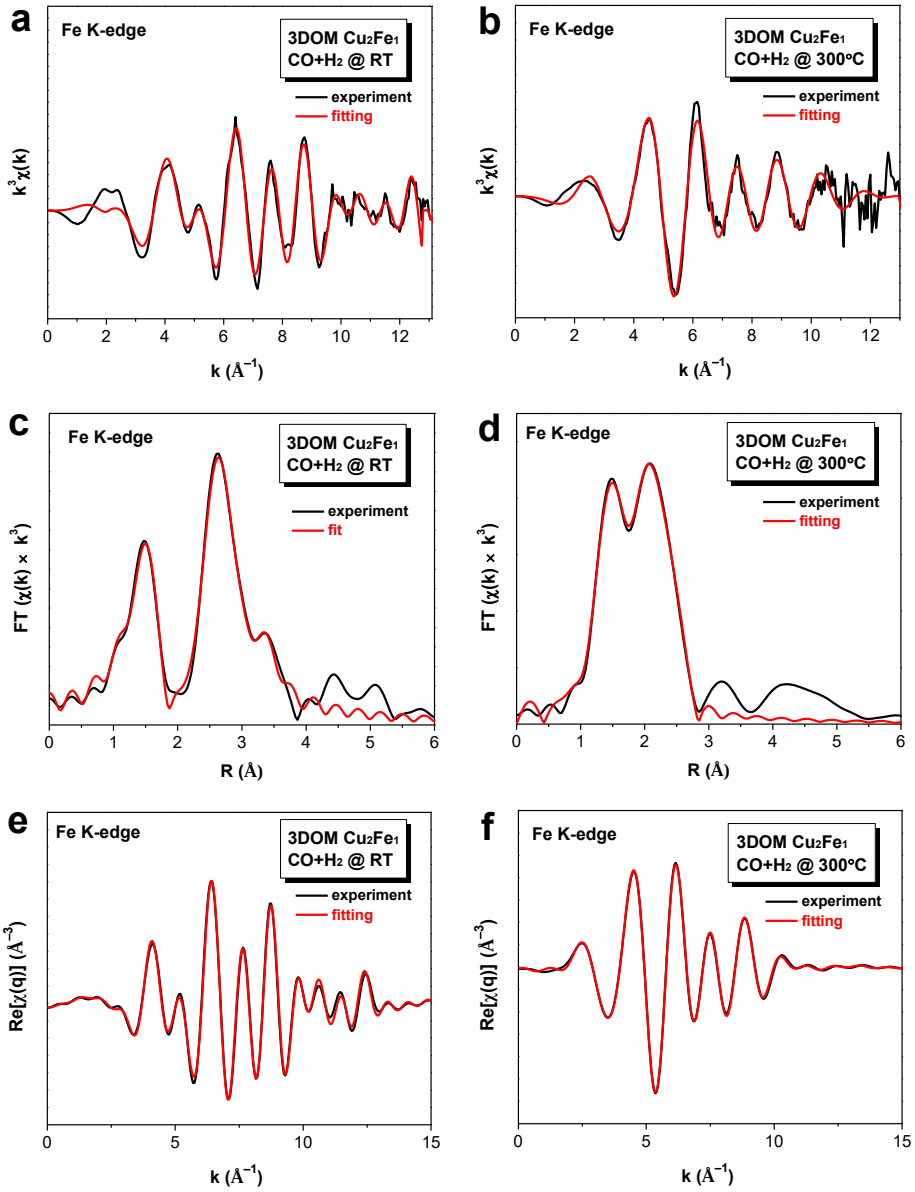

Figure S11. *In situ* $k^3\chi(k)$, Fourier transforms of [$k^3\chi(k)$] (R-space plot), and Re[χ(q)] (Å^{-3}) (q-space plot) spectra for the experimental Fe K-edge EXAFS signal of the 3DOM Cu_2Fe_1 catalyst at RT(a, c, e) and 300 ℃ (b, d, f) under CO+H_2 (H_2/CO = 1) gas and the fit (3DOM Cu_2Fe_1 CO+H_2@RT: Δk=3.4–12.6 Å^{-1} and ΔR=1.0–4.0 Å; 3DOM Cu_2Fe_1 CO+H_2@300℃: Δk=2.8–12.1 Å^{-1} and ΔR=1.0–3.0 Å).

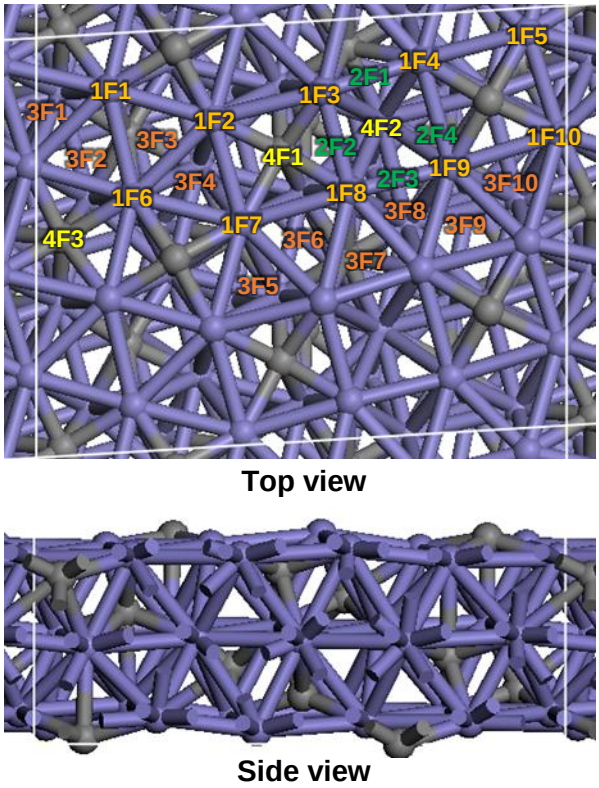

Figure S12. The χ-Fe_5C_2(510) surface morphology and its adsorption sites. The purple and gray balls denote Fe and C atoms, respectively.

The χ-Fe_5C_2(510) surface model. χ-Fe_5C_2 has a monoclinic structure with C2/c crystallographic symmetry,[2] including 20 Fe and 8 C atoms per unit cell. Our calculated lattice parameters (a = 11.588 Å, b = 4.579 Å, c = 5.059 Å, and β =97.7°) and magnetic moment (1.73 μB) agree well with the previous experimental data.[3,4] Zhao *et al*.[5] proved that χ-Fe_5C_2(510) surface with α=2.50 (α= Fe/C ratio) had low surface energy under synthesis gas pretreatment. Pham *et al*.[6] discovered that χ-Fe_5C_2(510) exhibited the largest percentage among the exposed crystal facets and the lowest surface energy among the stoichiometric terminations of 11 facets. Pham *et al*.[7] further revealed that CH_4 formation was unfavorable on χ-Fe_5C_2(510), and the reactions of C+CH and CH+CH were found the most likely coupling pathways in terms of the carbide mechanism. The surface morphology and adsorption sites of χ-Fe_5C_2(510) is illustrated in **Figure S12**.

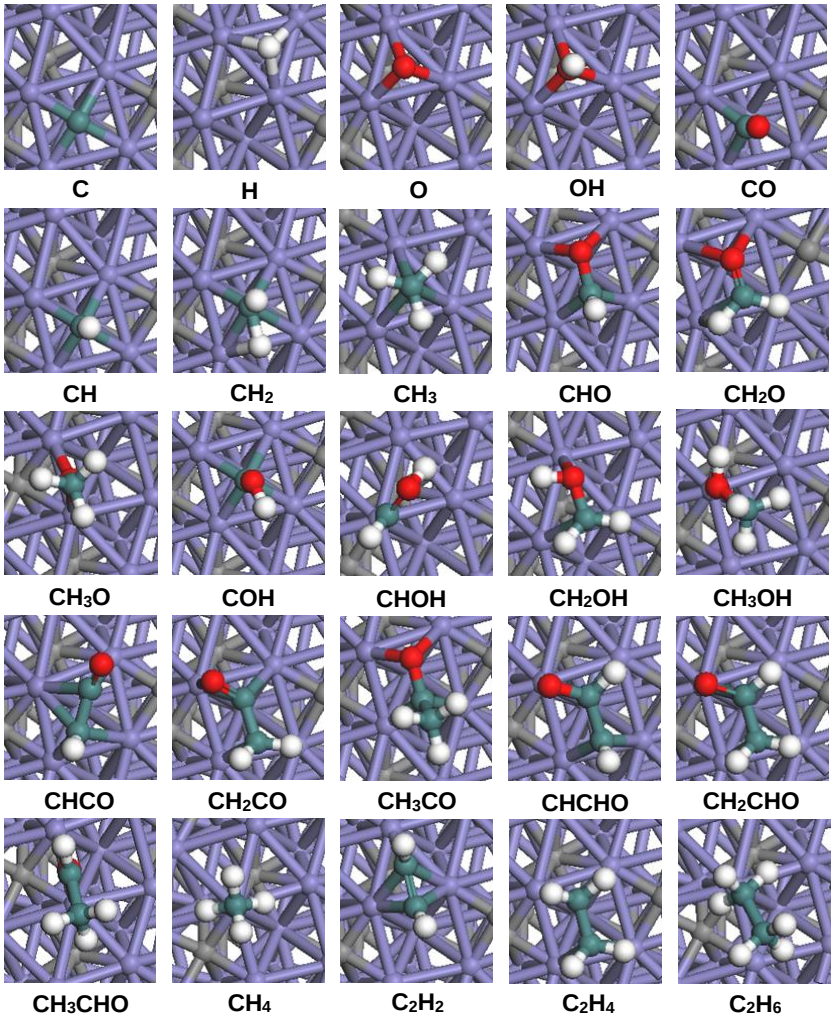

Figure S13. The most stable adsorption configuration of reactants, products and possible intermediates involved in CO hydrogenation to the formation of C_2 hydrocarbon and oxygenates on χ-Fe_5C_2(510) surface. Purple balls: Fe atoms; grey balls: C atoms on surface; dark green balls: C atoms involved in reactions; red balls: O atoms; white balls: H atoms.

The adsorption energy (E_{ads}/kJ·mol^{-1}) and key geometrical parameters (Å) of reactants and possible intermediates species involved in CO hydrogenation to the formation of C_2 hydrocarbons and oxygenates on χ-Fe_5C_2(510) surface are listed in **Table S7**. All possible elementary reactions involved in CO hydrogenation to the formation of C_2 hydrocarbons and oxygenates together with the activation energy (E_a) and reaction energy (ΔH) on χ-Fe_5C_2(510) surface are listed in **Table S8**.

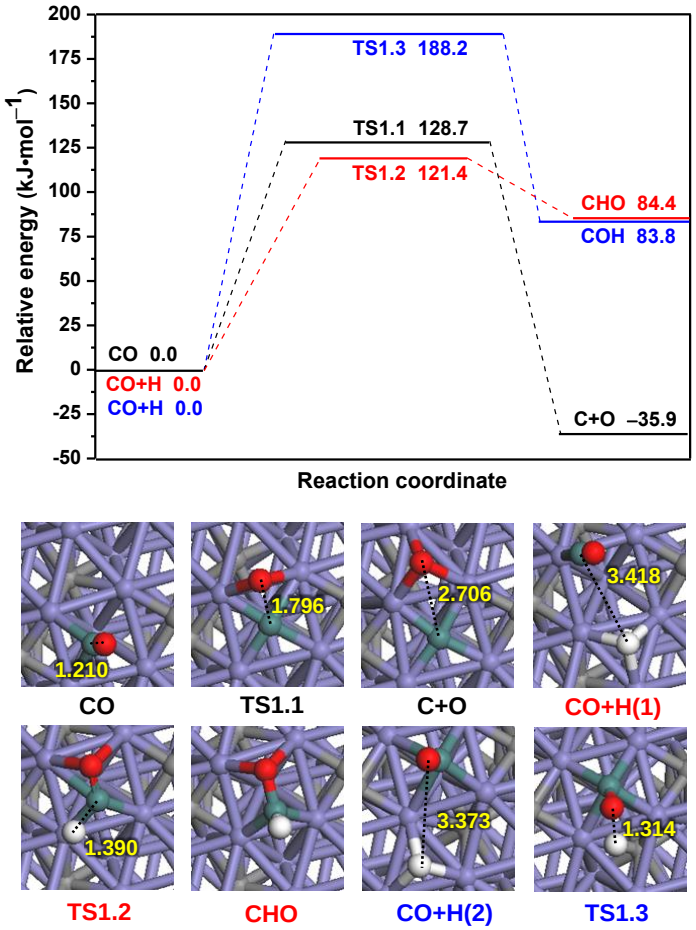

Figure S14. The potential energy diagram of CO activation together with the initial state (ISs), transition state (TSs) and final states (FSs) on χ-Fe_5C_2(510) surface. Bond lengths in Å. See **Figure S13** for color coding.

CO activation. Three possible elementary reactions (**Table S8**) on χ-Fe_5C_2(510) surface are examined: (**R1.1**) CO direct dissociation; (**R1.2**) CO hydrogenation to CHO; (**R1.3**) CO hydrogenation to COH. As shown in **Figure S14**, when CO and H are co-adsorbed on χ-Fe_5C_2(510) surface, the catalytic activity towards CO hydrogenation to COH is rather low. However, CO direct dissociation and CO hydrogenation to CHO are more favorable than CO hydrogenation to COH. Meanwhile, CO direct dissociation and CO hydrogenation to CHO are kinetically competitive due to their close activation barriers (128.7 vs. 121.4 KJ·mol^{-1}); whereas CO direct dissociation is favorable thermodynamically than CO hydrogenation to CHO (–35.9 *vs.* 84.4 KJ·mol^{-1}). Thus, C and CHO are the major products of CO initial step, CH_x (x = 1–3) formation starts with C and CHO intermediates.

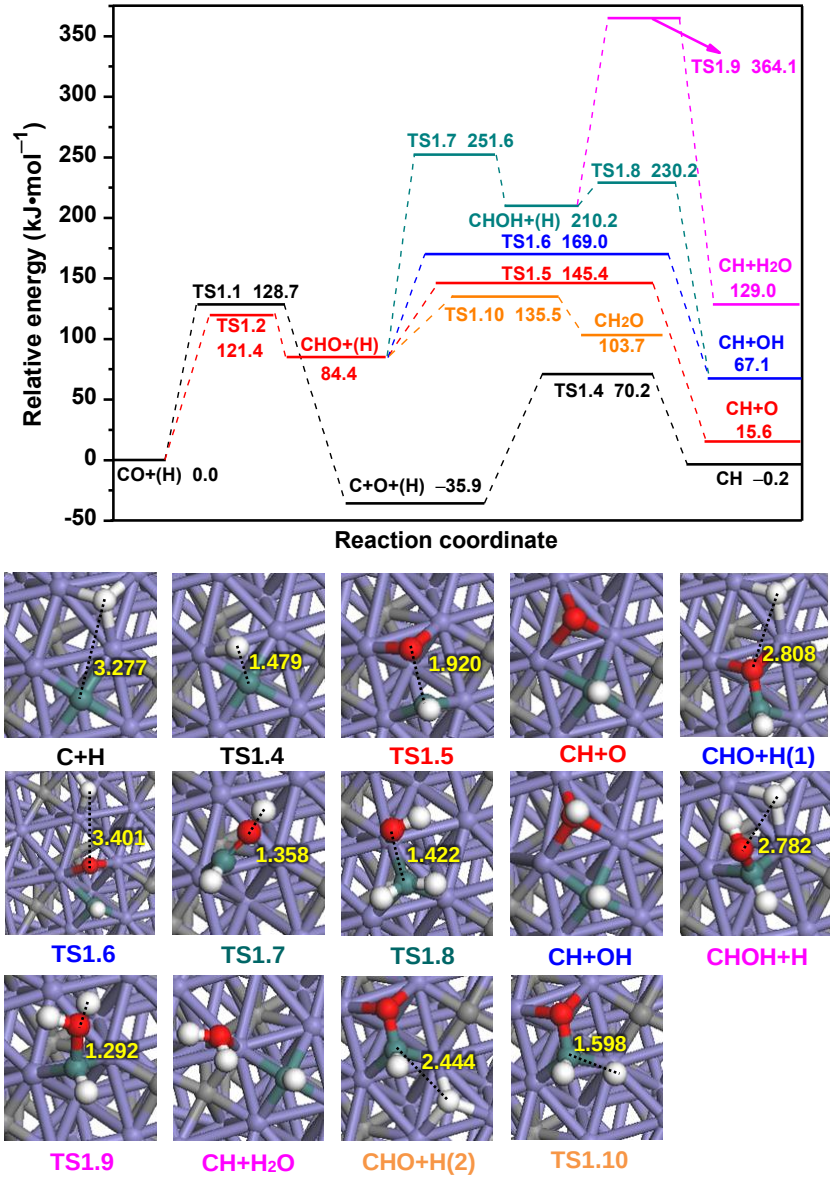

Figure S15. The potential energy diagram of CH and CH_2O formation together with the ISs, TSs and FSs on χ-Fe_5C_2(510) surface. Bond lengths in Å. See **Figure S13** for color coding.

CH Formation. C and CHO are the dominant products for CO initial step on χ-Fe_5C_2(510) surface. Thus, starting from C+H, CHO and CHO+H, five possible pathways with six elementary reactions (**R1.4**–**R1.9**) are responsible for CH formation (**Table S8**). Moreover, CHO hydrogenation to CH_2O (**R1.10**) is also considered. As illustrated in **Figure S15**, with respect to CO+H species, among five CH formation pathways, C hydrogenation to CH has the highest barrier of 128.7 kJ·mol^{-1} with the reaction energy of –0.2 kJ·mol^{-1}, which is more favorable both thermodynamically and kinetically than the other four pathways, suggesting that C hydrogenation to form CH via **TS1.1** (128.7 kJ·mol^{-1}) is dominantly responsible for CH formation, which is kinetically competitive with CHO hydrogenation to CH_2O via **TS1.10** (135.5 kJ·mol^{-1}). Whereas CH formation is favorable thermodynamically than CHO hydrogenation to CH_2O. In addition, our results indicate that C+C coupling reaction has a high activation barrier of 150.3 kJ·mol^{-1} with reaction energy of 118.9 kJ·mol^{-1}, which is higher than that of C hydrogenation to CH reaction with the activation barrier and reaction energy of 106.1 and 35.7 kJ·mol^{-1}, suggesting that C prefers hydrogenation to CH rather than C+C coupling.

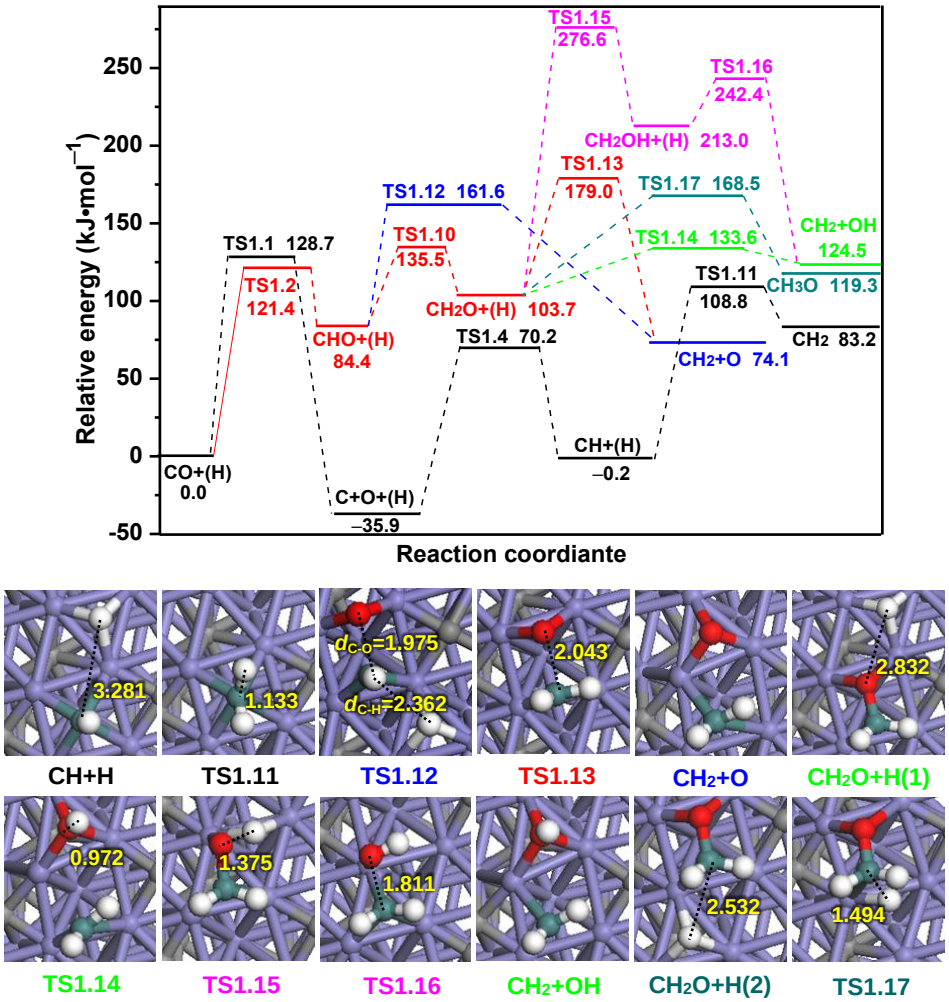

Figure S16. The potential energy diagram of CH_2 and CH_3O formation together with the ISs, TSs and FSs on χ-Fe_5C_2(510) surface. Bond lengths in Å. See **Figure S13** for color coding.

CH_2 formation. C and CHO prefer hydrogenation to CH and CH_2O, respectively. Starting from the initial states of CH+H, CHO+H and CH_2O, five possible pathways with six elementary reactions (**R1.11**–**1.16**) are responsible for CH_2 formation (**Table S8**). Meanwhile, CH_2O hydrogenation to CH_3O (**R1.17**) is also considered. As presented in **Figure S16**, with respect to CO+H species, among five possible pathways of CH_2 formation, both CH hydrogenation and CH_2O dissociation with H-assisted dominantly contribute to CH_2 formation with the highest barriers of 128.7 and 135.5 kJ·mol^{-1}, respectively. However, CH hydrogenation to CH_2 is more favorable thermodynamically than CH_2O dissociation with H-assisted to CH_2 (83.2 *vs.* 124.5 kJ·mol^{-1}). Moreover, CH_2 formation is also more favorable than CH_2O hydrogenation to CH_3O or CH_2OH, in which CH_2O prefers hydrogenation to CH_3O rather than CH_2OH.

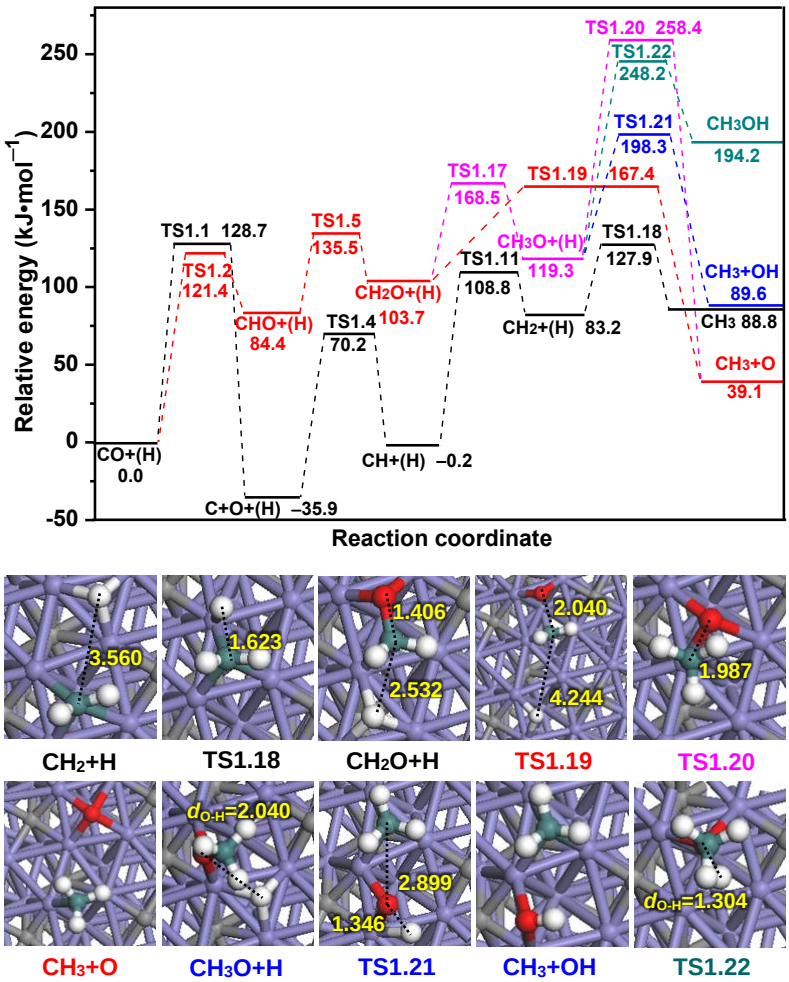

Figure S17. The potential energy diagram of CH_3 and CH_3OH formation together with the ISs, TSs and FSs on χ-Fe_5C_2(510) surface. Bond lengths in Å. See **Figure S13** for color coding.

CH_3 formation. Starting from the initial states of CH_2+H, CH_2O+H, and CH_3O, four possible pathways (**R1.18**–**1.21**) are responsible for CH_3 formation (**Table S8**). CH_3O hydrogenation to CH_3OH (**R1.22**) is also considered. As illustrated in **Figure S17**, with respect to CO+H species, among four CH_3 formation pathways, CH_2 hydrogenation to CH_3 has only the highest barrier of 128.7 kJ·mol^{-1}, which is dominantly responsible for CH_3 formation. Moreover, CH_3 formation is more favorable than CH_3OH formation.

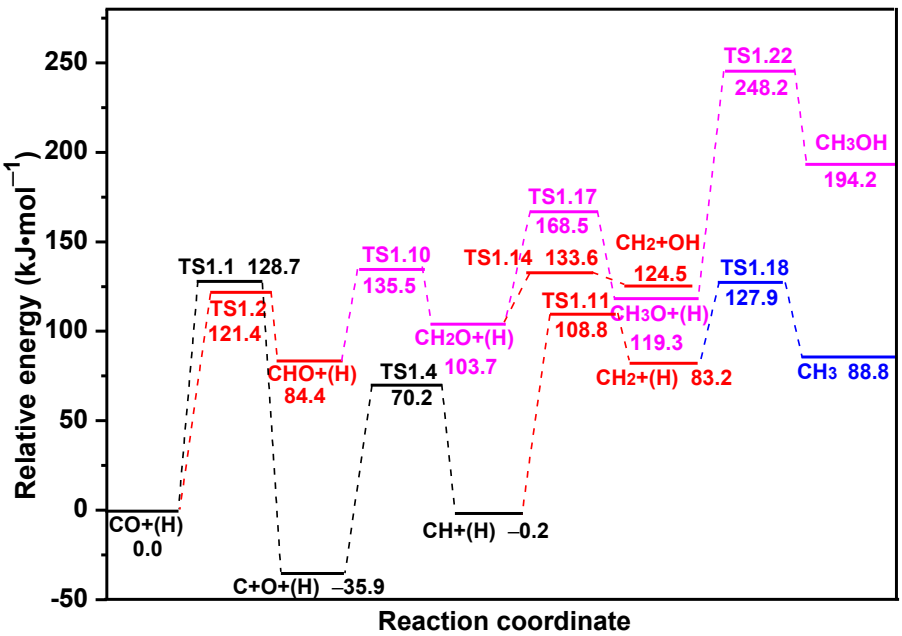

Figure S18. The potential energy diagram of the most favorable route for the formation of CH_x (x = 1–3) species and CH_3OH on χ-Fe_5C_2(510) surface.

Brief Summary of CH_x (x = 1–3) and CH_3OH. Starting from CO+H species, **Figure S18** presents the potential energy diagram for the most favorable formation pathways of CH_x (x = 1–3) species and CH_3OH. For CH formation, the reaction pathway of C+H→CH is more favorable than CHO→CH+O; for CH_2 formation, the pathways of C+H→CH+H→CH_2 and CHO+H→CH_2O+H→CH_2+OH are two parallel pathways; for CH_3 formation, the pathway of C+H→CH+H→CH_2+H→CH_3 is the most favorable. The pathway of CH_3OH formation is CHO+H→CH_2O+H→CH_3O+H→CH_3OH. CH (black line) and CH_3 (blue line) formation have the same highest barrier of 128.7 kJ·mol^{-1}. CH_2 formation (red line) via two parallel pathways have the highest barrier of 128.7 and 135.5 kJ·mol^{-1}, respectively. CH_3OH formation (pink line) had the highest barrier of 248.2 kJ·mol^{-1}, which is much higher than those of CH_x species formation, suggesting that CH_x species formation is much more favorable than CH_3OH formation, namely, χ-Fe_5C_2(510) surface exhibits good selectivity for CH_x (x = 1–3) species rather than CH_3OH in CO hydrogenation. In addition, Cao *et al.*[8] demonstrated that CH_3OH formation was also unfavorable on χ-Fe_5C_2(001) surface.

Therefore, among all CH_x (x = 1–3) species, CH is the dominant existence form on χ-Fe_5C_2(510) surface, which originates from CO direct dissociation into C, followed by C hydrogenation to CH. Moreover, CH hydrogenation also contributes to the formation of CH_2 and CH_3 species on χ-Fe_5C_2(510) surface. However, as menthioned behind, our results show that once CH_2 and CH_3 species are formed on χ-Fe_5C_2(510), both of them would dissociate into CH species among all reactions related to CH_x (x = 2, 3) species, which further comfirm that CH is the most favorable CH_x species.

The Formation of C_2-Hydrocarbons and C_2-Oxygenates. CH is the dominant species on χ-Fe_5C_2(510) surface. Moreover, CH_2 and CH_3 species can also be formed by CH hydrogenation. Thus, all possible reactions related to CH, CH_2 and CH_3 species including the dissociation, hydrogenation, coupling, and CO/CHO insertion are studied. **Figures S19–21** display the potential energy profile of these reactions related to CH, CH_2 and CH_3 species, respectively.

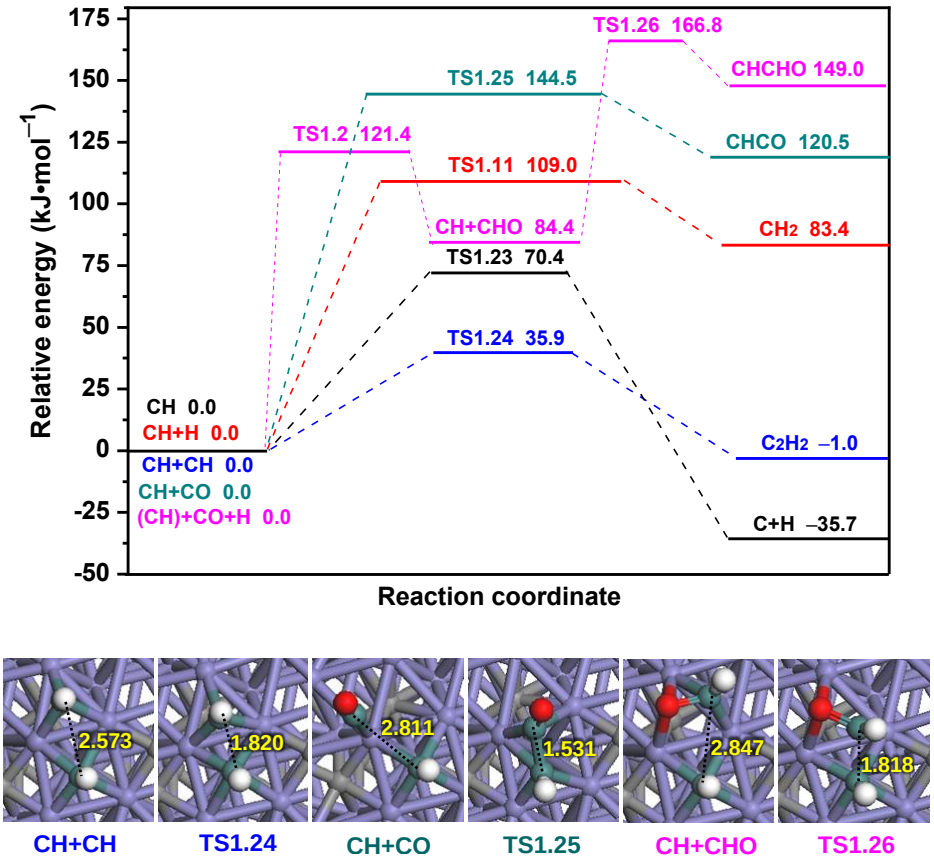

Figure S19. The potential energy diagram of the reactions related to CH species together with the ISs, TSs and FSs on χ-Fe_5C_2(510) surface. Bond lengths in Å. See **Figure S13** for color coding.

As illustrated in **Figure S19**, among all reactions related to CH species (**Table S8**), CH coupling to C_2H_2 (**R1.24**) is the most favorable with the activation barrier and reaction energy of 35.9 and –1.0 kJ·mol^{-1}, respectively. The second is CH dissociation into C and H atoms (**R1.23**), this reaction has an activation barrier of 70.4 kJ·mol^{-1} with reaction energy of –35.7 kJ·mol^{-1}. CH hydrogenation to CH_2 (**R1.11**), CO insertion into CH to form CHCO (**R1.25**), are less favorable due to their high activation barriers of 109.0 and 144.5, respectively. Furthermore, CHO insertion into CH to form CHCHO (**R1.26**) is difficult to occur due to its high activation barriers of 166.8 kJ·mol^{-1} with reaction energy of 149.0 kJ·mol^{-1}.

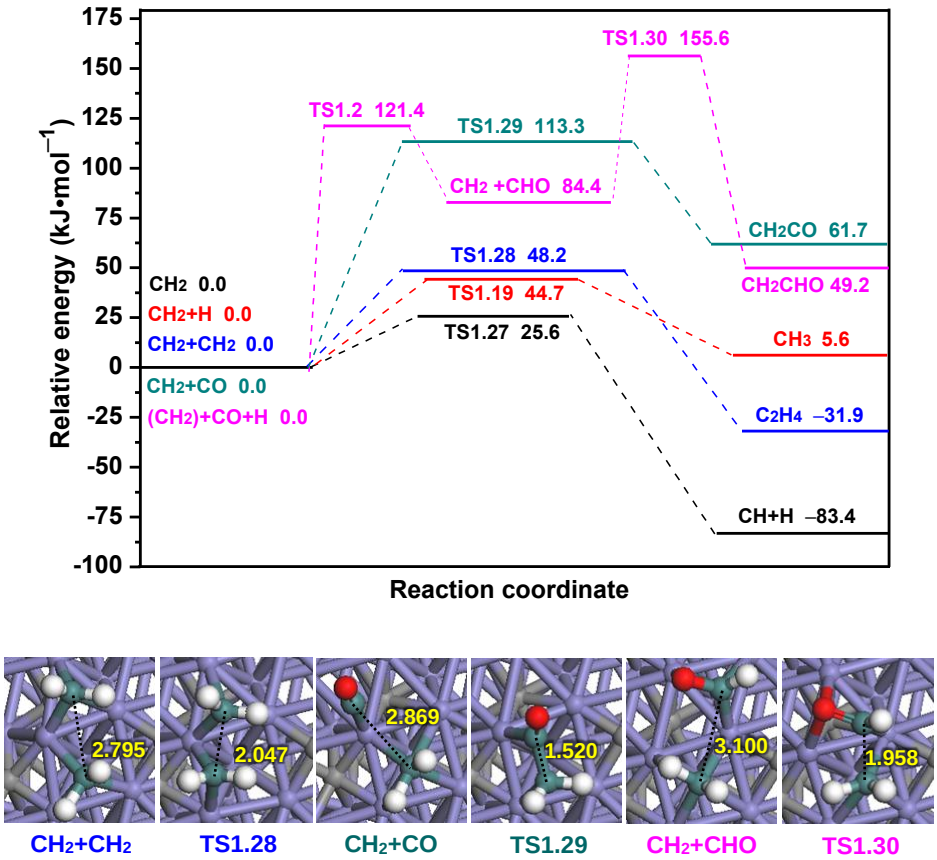

Figure S20. The potential energy diagram of the reactions related to CH_2 species together with the ISs, TSs and FSs on χ-Fe_5C_2(510) surface. Bond lengths in Å. See **Figure S13** for color coding.

As shown in **Figures S20–21**, among all reactions related to CH_2 and CH_3 species, the calculation results indicate that CH_2 and CH_3 prefer dissociation into CH and CH_2 species with the activation barriers of 25.6 and 39.0 kJ·mol^{-1}, respectively. This means that once CH_2 and CH_3 species are formed, both of them would dissociate into CH species. This result further confirms that CH is the most favorable CH_x species on χ-Fe_5C_2(510) surface. In addition, previous studies demonstrated that CH and CH_2 species are the most favorable CH_x species on χ-Fe_5C_2(010) surface,[9] as well as CH and CH_3 are the most favorable CH_x species on χ-Fe_5C_2(001) surface.[10] Furthermore, CHO insertion into CH_2/CH_3 to form CH_2CHO/CH_3CHO (**R1.30/R1.35**) are difficult to occur due to their high activation barriers of 155.6 and 216.5 kJ·mol^{-1} with reaction energy of 49.2 and 144.1 kJ·mol^{-1}, respectively.

The above-mentioned results indicate that starting from the most favorable CH species, CH coupling to C_2H_2 is the most favorable reaction to form C_2-hydrocarbons rather than its dissociation to C (**TS1.23**), hydrogenation to CH_2 (**TS1.11**), or being inserted by CO/CHO (**TS1.25**, **TS1.26**) to form C_2-oxygenates on χ-Fe_5C_2(510) surface.

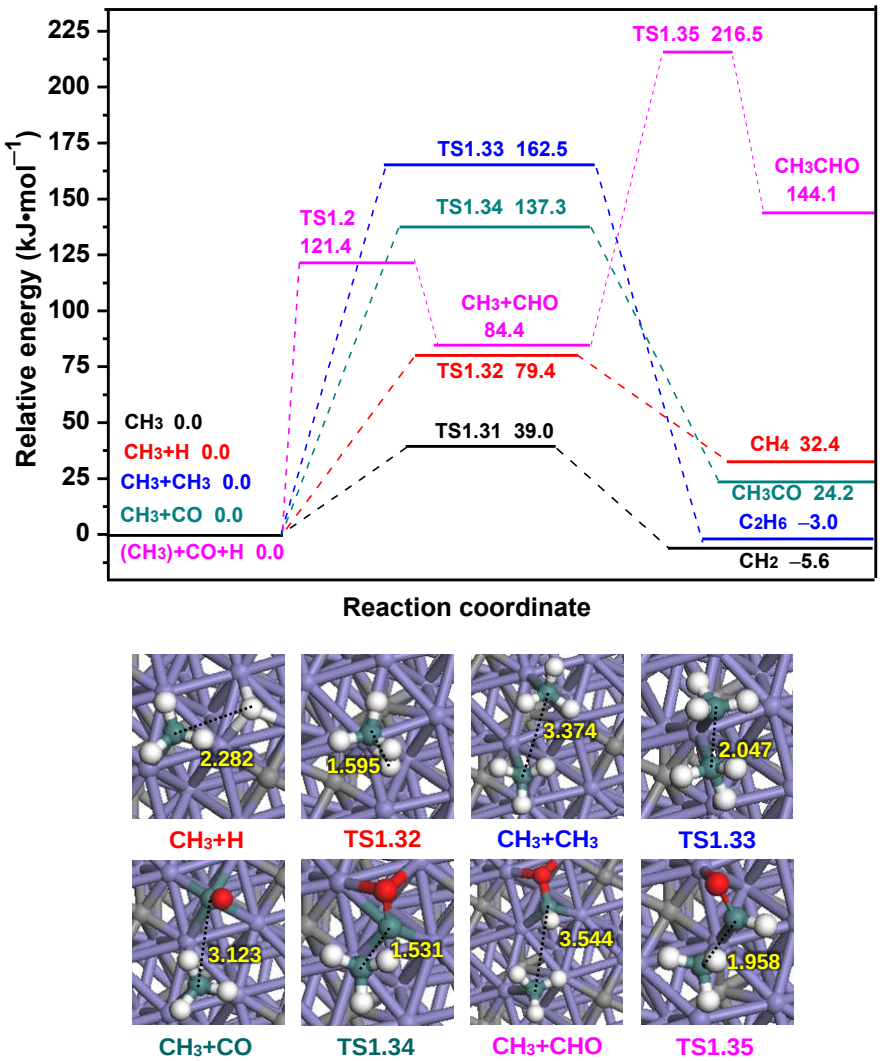

Figure S21. The potential energy diagram of the reactions related to CH_3 species together with the ISs, TSs and FSs on χ-Fe_5C_2(510) surface. Bond lengths in Å. See **Figure S13** for color coding.

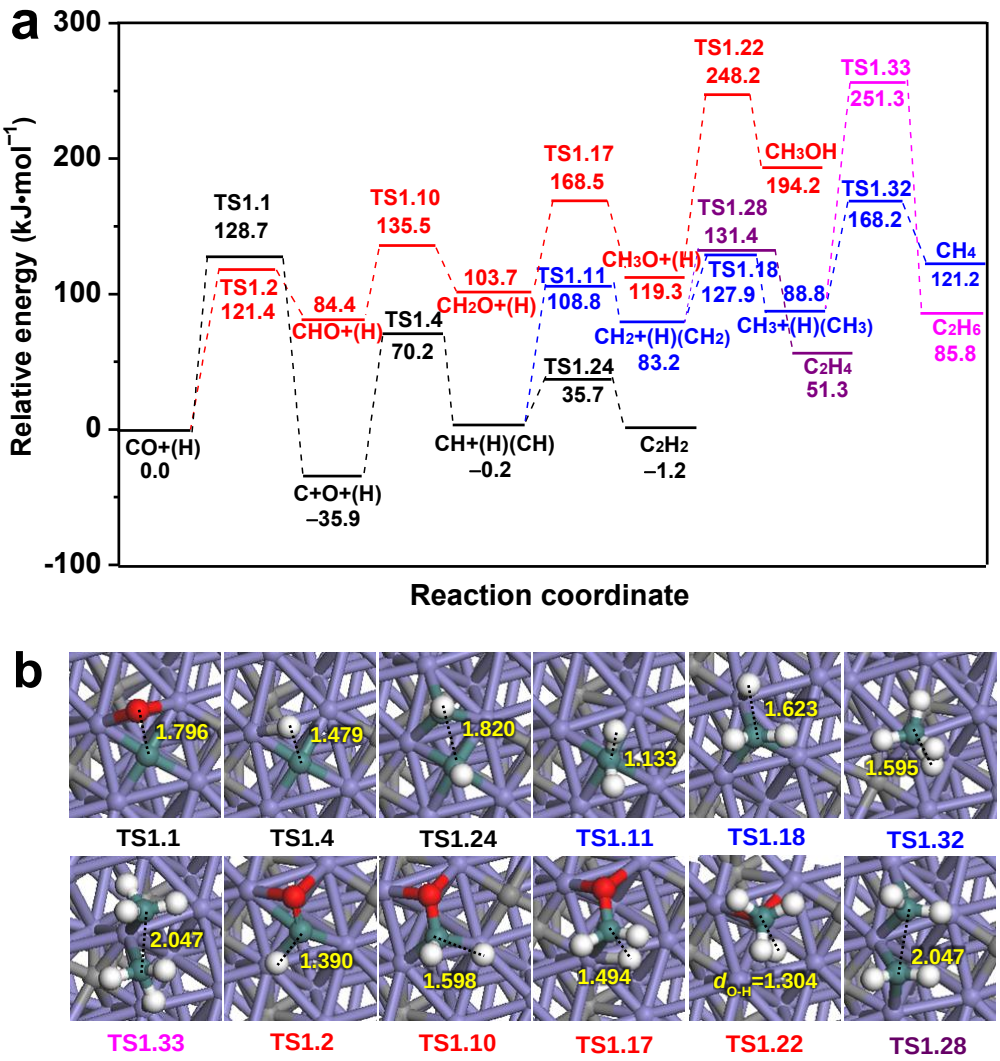

Figure S22. The optimal CO hydrogenation reaction pathway and transition states (TSs) on χ-Fe_5C_2(510) surface. (a) The optimal reaction pathway for CO hydrogenation on χ-Fe_5C_2(510) surface (unit: kJ·mol^{-1}). (b) Top view of TSs involved in the reaction shown in panel (a). Bond lengths in Å. See **Figure S13** for color coding.

CO hydrogenation on χ-Fe_5C_2(510). The reaction pathway for CO hydrogenation on χ-Fe_5C_2(510) is presented in **Figure S22**. On χ-Fe_5C_2(510), CO direct dissociation via **TS1.1** and CO hydrogenation to CHO via **TS1.2** are more favorable than CO hydrogenation to COH (**Figure S14**). Meanwhile, CO direct dissociation (**TS1.1**, 128.7 kJ·mol^{-1}) and CO hydrogenation to CHO (**TS1.2**, 121.4 kJ·mol^{-1}) are kinetically competitive due to their close activation barriers. C and CHO are thus the major intermediates of CO activation. Starting from the initiate states of C+H, CHO, and CHO+H, C hydrogenation to CH via **TS1.4** is more favorable than the other pathways (**Figure S15**). This suggests that C hydrogenation is dominantly responsible for CH formation (**TS1.1**, 128.7 kJ·mol^{-1}), which is kinetically competitive with CH_2O formation

via **TS1.10** (135.5 kJ·mol^{-1}). Starting from the initiate states of CH+H, CHO+H, and CH_2O, both CH hydrogenation (**TS1.11**) and CH_2O dissociation with H-assisted significantly contribute to CH_2 formation (**Figure S16**). Furthermore, CH_2 formation is more favorable than CH_3O (**TS1.17**) or CH_2OH (**TS1.15**), in which CH_2O prefers hydrogenation to CH_3O rather than CH_2OH (**Figure S16**). Starting from the initial states of CH_2+H, CH_2O+H, and CH_3O, CH_2 hydrogenation (**TS1.18)** mainly results in CH_3 formation, which is more favorable than CH_3OH formation via **TS1.22** (**Figure S17**). CH is thus the most favorable CH_x (x=1–3) species on χ-Fe_5C_2(510) (**Figure S18**). Additionally, CH formation (**TS1.1**, **TS1.4**) is more favorable than CH_3OH formation (**TS1.2, TS1.10, TS1.17, TS1.22**), suggesting that χ-Fe_5C_2(510) exhibits higher selectivity to CH instead of CH_3OH (**Figures S18** and **Figure S22**).

CH coupling to C_2H_2 via **TS1.24** is the most favorable reaction rather than its dissociation to C, hydrogenation to CH_2, or being inserted by CO/CHO to C_2-oxygenates on χ-Fe_5C_2(510) (**Figure S19**). CH_2 prefers dissociation into CH species rather than hydrogenation to CH_3, coupling to C_2H_4 (**TS1.28**), or being inserted by CO/CHO to C_2-oxygenates (**Figure S20**). CH_3 prefers dissociation into CH_2 species instead of hydrogenation to CH_4 (**TS1.32**), coupling to C_2H_6 (**TS1.33**), or being inserted by CO/CHO to C_2-oxygenates (**Figure S21**). Once CH_2 and CH_3 species are formed on χ-Fe_5C_2(510), both would dissociate to CH species, which further confirm that CH is the most favorable CH_x (x = 1–3) species. The calculation results are in excellent agreement with the experimental results[11,12] and DFT calculations[5,6,13] that χ-Fe_5C_2 exhibits good catalytic performance for CO dissociation[14] and carbon-chain propagation for Fe-based FTS catalysts. Thus, CH is the most favorable species on χ-Fe_5C_2(510), and χ-Fe_5C_2(510) mainly contributes to the formation of C_2H_2 via CH coupling (**Figure S22**, **Supplementary Movie 1**).

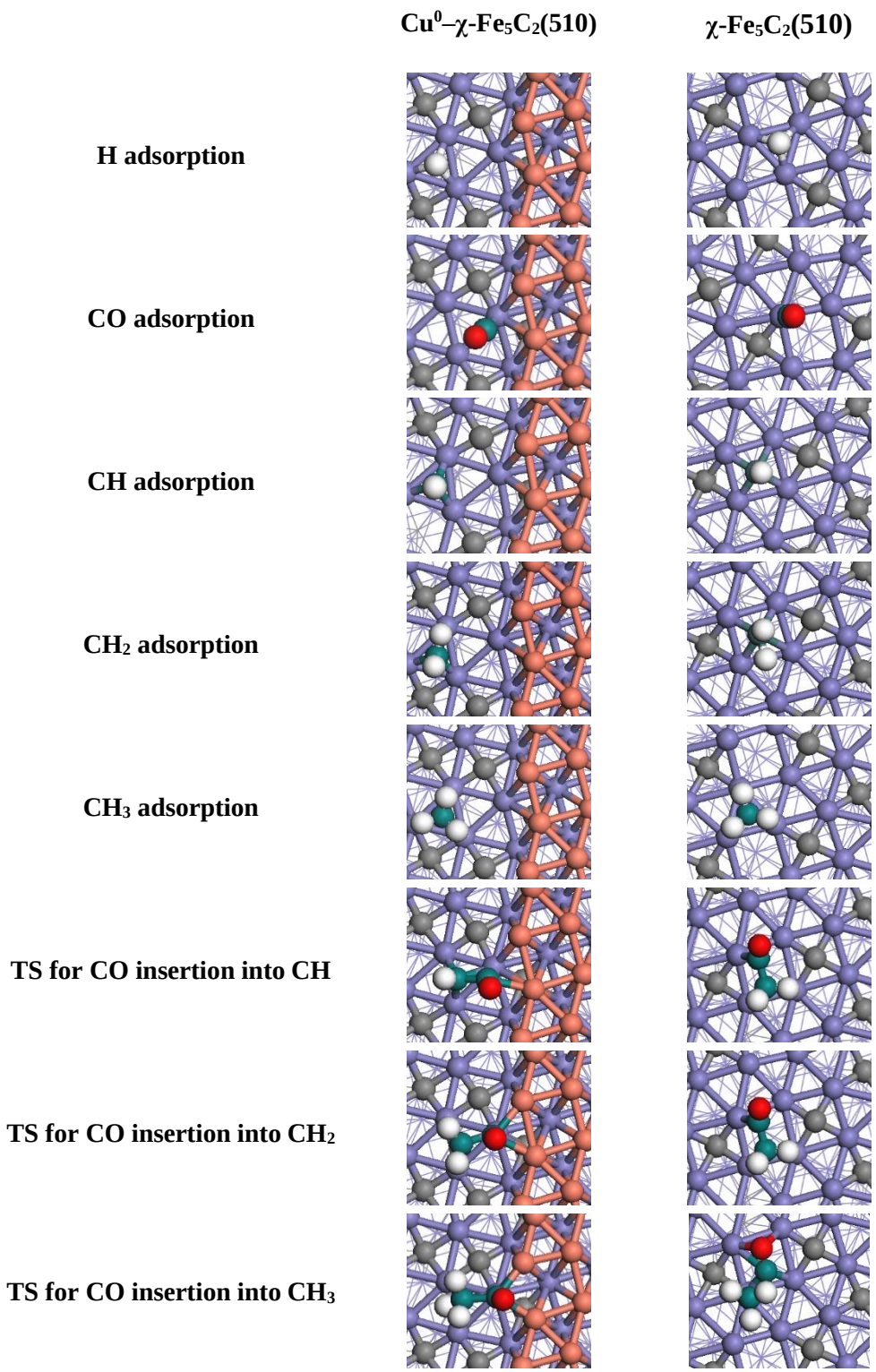

Figure S23. Structural information for the adsorption of CH_x (x = 1–3), H and CO species, as well as the transition states for CO insertion into CH_x (x = 1–3) on Cu^0–χ-Fe_5C_2(510) and χ-Fe_5C_2(510) surface. Purple, red, white and orange balls denote Fe, O, H and Cu atoms, respectively. Gray and dark green balls present the C atoms of χ-Fe_5C_2(510) surface and the C atoms of adsorbed species, respectively.

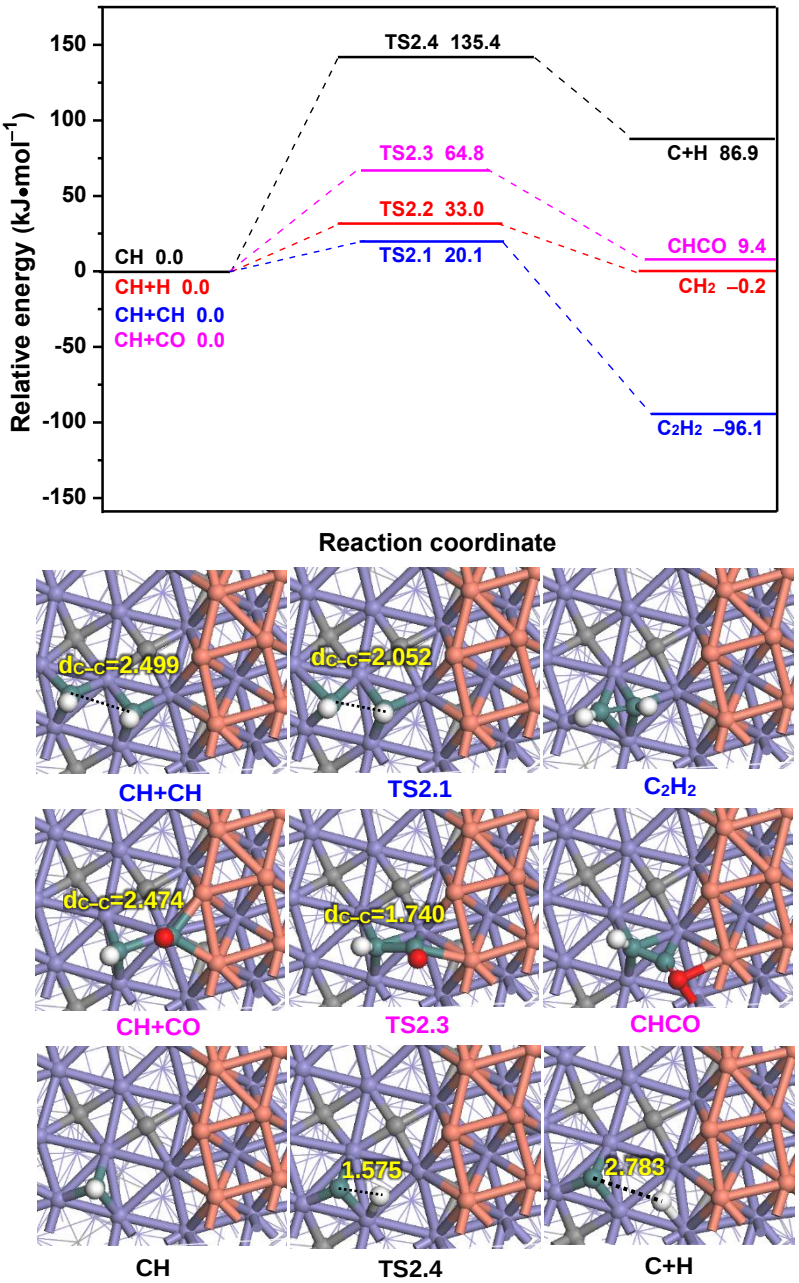

Figure S24. The potential energy diagram of the reactions related to CH together with the ISs, TSs and FSs on Cu^0–χ-Fe_5C_2(510). Bond lengths are in Å. See **Figure S23** for color coding.

For CH species (**Figure S24**), CH coupling to C_2H_2 via **TS2.1** is the most favorable reaction, which has the smallest activation barrier and reaction energy of 20.1 and –96.1 kJ·mol^{-1}, respectively; in **TS2.1**, two CH species are adsorbed at two 3-fold Fe sites, respectively; the C–C distance decreases to 2.052 Å from 2.499 Å in CH+CH. The second favorable reaction is CH hydrogenation to CH_2 via **TS2.2**, this elementary reaction has an activation barrier of 33.0 kJ·mol^{-1} with a reaction energy of –0.2 kJ·mol^{-1}; since this reaction is the reverse reaction of CH_2 dissociation into CH and H, **TS2.2** is the same with **TS2.7** in **Figure S25**. The third is CO insertion into CH to CHCO via **TS2.3**, this elementary reaction has an activation barrier of 64.8 kJ·mol^{-1} with a reaction energy of 9.4 kJ·mol^{-1}; in **TS2.3**, CH is adsorbed at the 3-fold Fe site, and CO is adsorbed at the Cu–Fe bridge B_I2 site of Fe–Cu interface; the C–C distance decreases to 1.740 Å from 2.474 Å in CH+CO. Finally, CH dissociation into C and H atoms via **TS2.4** is difficult to occur due to the high activation barrier of 135.4 kJ·mol^{-1} with a reaction energy of 86.9 kJ·mol^{-1}; in **TS2.4**, C and H are adsorbed at the 3-fold F2 Fe site and the top T4 Fe sites, respectively; the C–H distance is 1.575 Å.

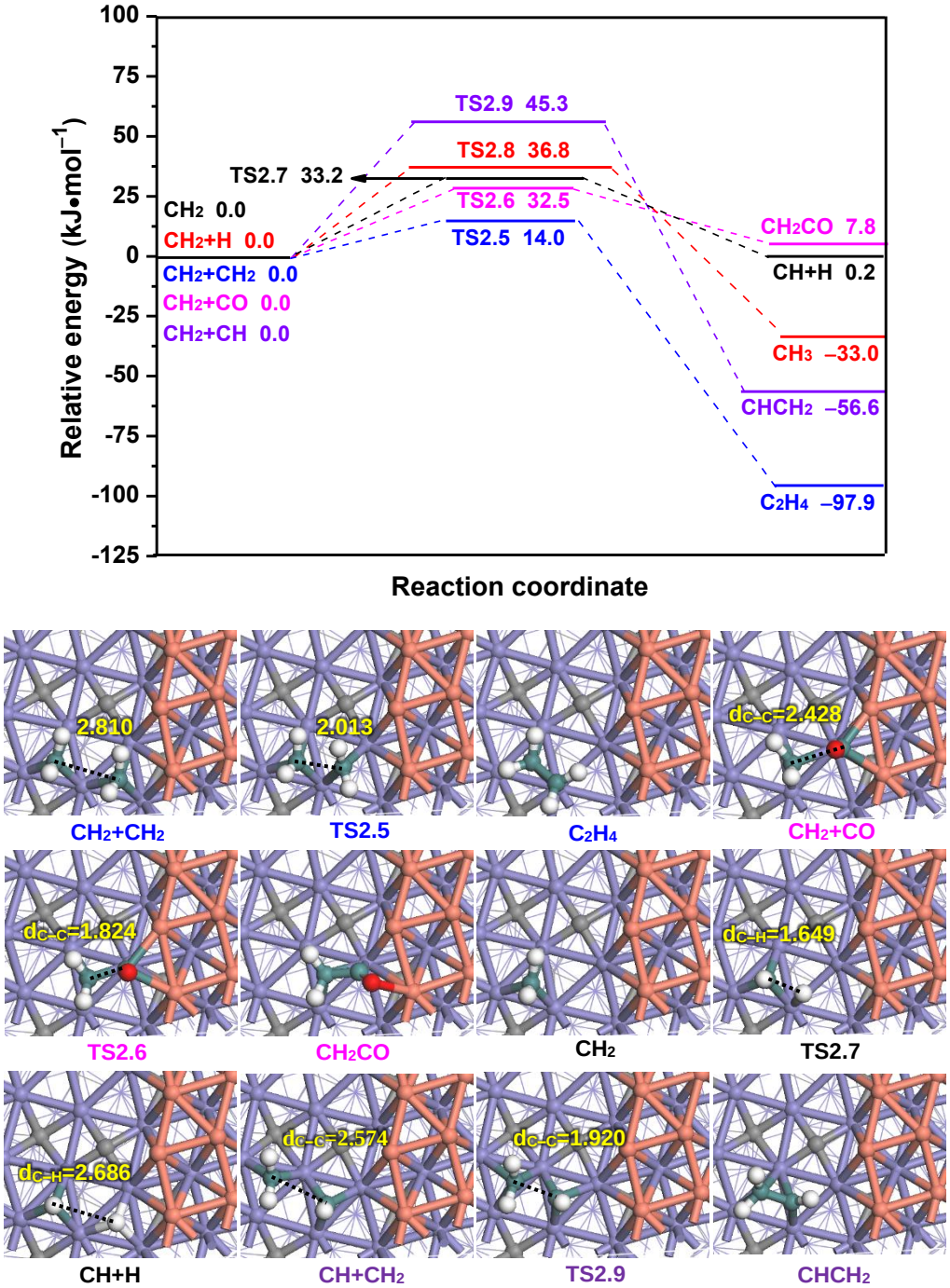

Figure S25. The potential energy diagram of the reactions related to CH_2 together with the ISs, TSs and FSs on Cu^0–χ-Fe_5C_2(510). Bond lengths are in Å. See **Figure S23** for color coding.

For CH_2 species, as presented in **Figure S25**, CH_2 coupling to C_2H_4 via **TS2.5** has the smallest activation barrier of 14.0 kJ·mol^{-1} with a reaction energy of –97.9 kJ·mol^{-1}; in **TS2.5**, two CH_2 are adsorbed at the 3-fold F2 Fe and the Fe–Fe bridge sites, respectively; the C–C distance decreases to 2.013 Å from 2.810 Å in CH_2+CH_2.

The second is CO insertion into CH_2 to CH_2CO via **TS2.6**, this elementary reaction has an activation barrier of 32.5 kJ·mol^{-1} with a reaction energy of 7.8 kJ·mol^{-1}; in **TS2.6**, CH_2 is adsorbed at the 3-fold F3 Fe site, and CO is adsorbed at the 3-fold F_I1 site of Fe–Cu interface with the C–C distance decreases to 1.824 Å from 2.428 Å in CH_2+CO.

Compared to CO insertion, CH_2 dissociation into CH and H via **TS2.7** has the comparable activation barrier of 33.2 kJ·mol^{-1}; in **TS2.7**, CH and H are adsorbed at the 3-fold F2 Fe site and the top T4 Fe site with the C–H distance of 1.649 Å. Moreover, CH_2 hydrogenation to CH_3 via **TS2.8** has the activation barrier of 36.8 kJ·mol^{-1} with the reaction energy of –33.0 kJ·mol^{-1}; since this reaction is the reverse reaction of CH_3 dissociation into CH_2 and H, **TS2.8** is the same with **TS2.10** in **Figure S26**.

In addition, as shown **Figures S25–26**, since both CH and CH_2 are the most favorable CH_x species on Cu^0–χ-Fe_5C_2(510) surface, CH_2 coupling with CH to $CHCH_2$ has also been considered. Our calculation results show that CH coupling with CH_2 via **TS2.9** has an activation barrier of 45.3 kJ·mol^{-1} with a reaction energy of –56.6 kJ·mol^{-1}; in **TS2.9**, CH and CH_2 are adsorbed at 3-fold F3 Fe site and 3-fold F1 Fe site, respectively, and the C–C distance decreases to 1.920 Å from 2.574 Å in CH+CH_2.

The above results show that CH_2 coupling to C_2H_4 via **TS2.5** is the most favorable; then, CH_2CO is formed via **TS2.6** by CO insertion into CH_2. However, under the real Fischer–Tropsch synthesis conditions, CO as the reactant is the abundant surface species, for example, CO adsorption reaches 0.5 ML on Cu(100) surface[15] and different Fe surfaces[16] under high temperature and pressure. Thus, although CH_2 coupling is faster than CO insertion in the view of kinetics, CO insertion into CH_2 to C_2-oxygenate (CH_2CO) can be accelerated due to the abundant coverage of CO and the small activation barrier difference of 18.5 kJ·mol^{-1} between CH_2 coupling and CO insertion reactions.

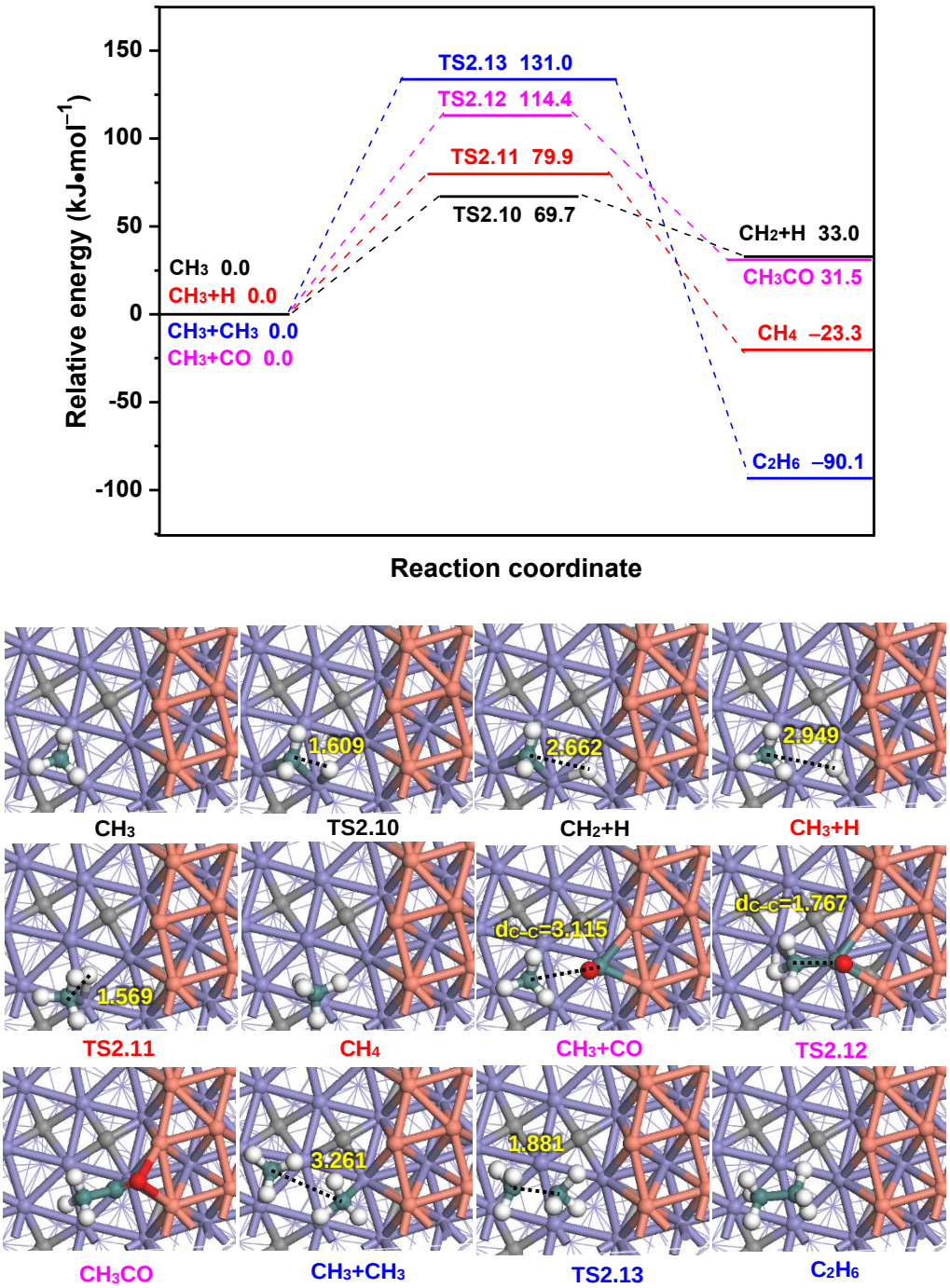

Figure S26. The potential energy diagram of the reactions related to CH_3 together with the structures (ISs, TSs and FSs on Cu^0–χ-Fe_5C_2(510) surface. See **Figure S23** for color coding.

As shown in **Figure S26**, among all reactions related to CH_3 species, CH_3 prefers dissociation to CH_2 via **TS2.10** with an activation barrier and reaction energy of 69.7 and 33.0 kJ·mol^{-1}, respectively; in **TS2.10**, CH_2 is adsorbed at the F2 Fe site, and H is adsorbed at the T4 Fe site; the C–H distance is 1.609 Å.

Then, CH_3 hydrogenation to CH_4 via **TS2.11** needs to overcome an activation barrier of 79.9 kJ·mol^{-1} with a reaction energy of –23.3 kJ·mol^{-1}; in **TS2.11**, both CH_3 and H are adsorbed at the T4 Fe site via both Fe–C and Fe–H bonds; the C–H distance decreases to 1.569 Å from 2.949 Å in CH_3+H.

CO insertion into CH_3 to CH_3CO via **TS2.12** has an activation barrier of 114.4 kJ·mol^{-1} with a reaction energy of 31.5 kJ·mol^{-1}. In **TS2.12**, CH_3 is adsorbed at the 3-fold F3 Fe site, and CO is adsorbed at the 3-fold F_I1 site of Fe–Cu interface; the C–C distance decreases to 1.767 Å from 3.115 Å in CH_3+CO.

Further, CH_3 coupling to C_2H_6 via **TS2.13** is difficult to occur due to the high activation barrier of 131.0 kJ·mol^{-1}. In **TS2.13**, two CH_3 are adsorbed at two Fe–Fe bridge sites with the C–C distance of 1.881 Å.

The above results show that CH_3 coupling to C_2H_6 via **TS2.13** and CO insertion into CH_3 to CH_3CO via **TS2.12** are difficult to occur due to the high activation barriers (131.0 and 114.4 kJ·mol^{-1}); namely, CH_3 species cannot contribute to the formation of C_2-hydrocarbons and C_2-oxygenates. As a result, once CH_3 appears over Cu^0–χ-Fe_5C_2(510) surface, it prefers dissociation to CH_2 species.

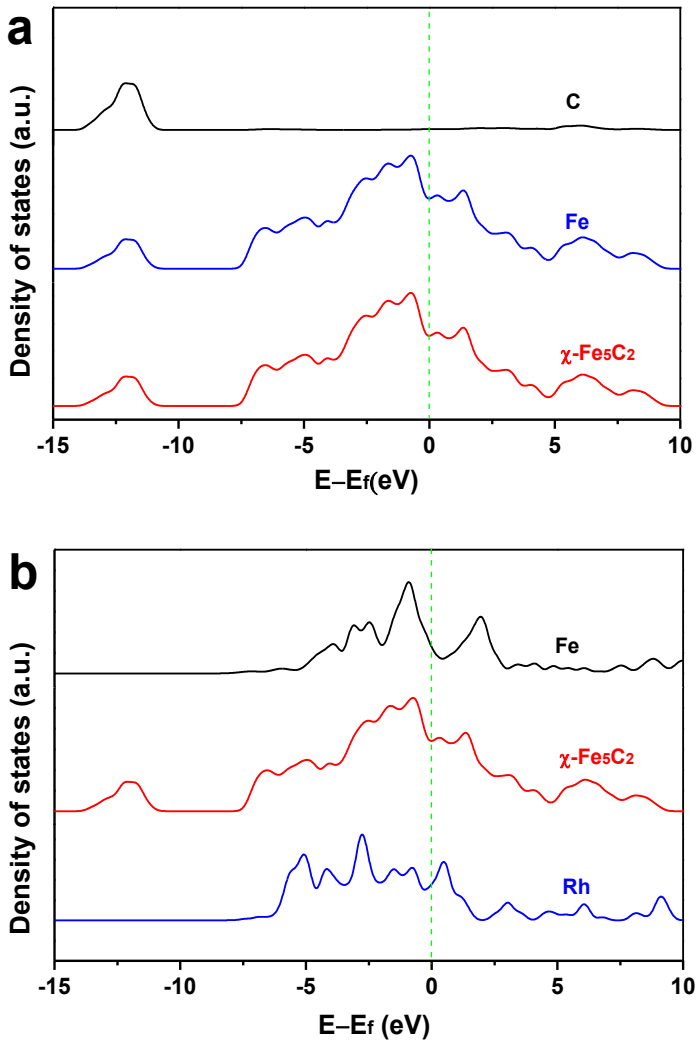

Figure S27. (a) Calculated partial density of state for χ-Fe_5C_2 projected at C and Fe sites and total densities of state for χ-Fe_5C_2. (b) Density of states of bulk Fe, χ-Fe_5C_2 and Rh. The green dash line is the Fermi level.

The χ-Fe_5C_2 phase has a monoclinic structure with *C*2/*c* crystallographic symmetry, and the Fe−Fe distances in bulk χ-Fe_5C_2 (2.52 and 2.71 Å) are 2%–9% larger than those (2.48Å) in the metal Fe.[2] The calculated density of states (**Figure S27**) shows that χ-Fe_5C_2 is metallic in nature, where Fe is a cation with a Bader charge of 0.40 *e*, and C is anion with Bader charge of –0.99*e*.

Table S1. The chain growth probability (α) of 1-alcohols and hydrocarbons (including olefins and paraffins) over 3DOM Cu-Fe catalysts at 200 ℃.

	Chain growth probability (α) for various catalysts				
	3DOM Fe	3DOM Cu_1Fe_2	3DOM Cu_1Fe_1	3DOM Cu_2Fe_1	3DOM Cu_3Fe_1
1-alcohols	0.83	0.75	0.78	0.81	0.76
Hydrocarbons	0.86	0.80	0.82	0.83	0.81

Table S2. The chain growth probability (α) of 1-alcohols and hydrocarbons (including olefins and paraffins) over 3DOM Cu_2Fe_1 catalyst at different temperatures (200–280℃).

	Chain growth probability (α) for 3DOM Cu_2Fe_1 catalysts				
	200 ℃	220 ℃	240 ℃	260 ℃	280 ℃
1-alcohols	0.81	0.78	0.74	0.71	0.70
Hydrocarbons	0.83	0.80	0.78	0.75	0.73

Table S3. Catalytic performance of 3DOM Cu_2Fe_1 catalysts in comparison to silica-supported Rh-based catalysts.

Catalysts [a]	H_2/CO	T (°C)	P (psig)	GHSV (h^{-1})	X_{CO} [e] (%)	S_{MeOH} [f] (%)	$S_{C_{2+}Oxy}$ [g] (%)	S_{HC} [h] (%)	S_{CO_2} [i] (%)	$r_{C_{2+}OH}$ [j]	Ref.
3DOM Cu_2Fe_1	1	260	700	2000	58.4	5.2	26.1(26.1)	57.2	11.5	5.65	This work
Rh(5)/SiO_2 [b]	1	260	700	2000	6.3	1.8	28.5(11.2)	68.9	0.8	0.63	–
Rh(1.5)/SiO_2	2	270	435	4000	5.0	1.4	15.3(8.90)	81.8	0	N.A.	17
Rh(5.6)Mn(1.7)/SiO_2	1.9	256	1200	7500 [c]	2.62	1.5	34.3(12.4)	64.2	0	N.A.	18
Rh(1.5)Mn(0.4)/SiO_2	2	270	435	4000	17.0	0.8	46.1(19.5)	52.4	0.7	N.A.	17
Rh(3)Mn(1)/SiO_2	2	285	290	N.A.	36.4	0	42.9(14.6)	54.1	0	N.A.	19
Rh(1.5)Mn(1.5) Li(0.07)Fe(0.1)/SiO_2	2	300	435	10000 [d]	28.2	0.6	58.2(22.9)	39.8	1.4	N.A.	20

[a]: The values shown in brackets are used as weight percent. [b]: Catalyst was prepared by using an impregnation method. [c]: Space velocity in L L_{cat}^{-1} h^{-1}. [d]: Space velocity in mL g_{cat}^{-1} h^{-1}. [e]: X_{CO} denotes CO conversion. [f]: S_{MeOH} denotes the selectivity to methanol. [g]: $S_{C_{2+}Oxy}$ denotes the selectivity to C_{2+} oxygenates. The selectivity to higher alcohols ($C_{2+}OH$) is expressed in brackets. [h]: S_{HC} denotes the selectivity to hydrocarbons. [i]: S_{CO_2} denotes the selectivity to CO_2. [j]: $r_{C_{2+}OH}$ denotes the formation rate of higher alcohols in mmol g_{cat}^{-1} h^{-1}.

Table S4. The texture characteristics, the formation rate of $C_{2+}OH$, and the intrinsic activity of the reduced catalyst samples.

Sample after reduction [a]	S_{BET} [c] ($m^2\ g^{-1}$)	V_{pore} [d] ($cm^3\ g^{-1}$)	d_{pore} [e] (nm)	$r_{C_{2+}OH}$ (mmol $g_{cat}^{-1}\ h^{-1}$)	Intrinsic activity [f] (mmol $m^{-2}\ h^{-1}$)
3DOM Cu	8.69	0.025	11.5	0	0
3DOM Cu_1Fe_2	74.7	0.358	19.2	1.76	2.4×10^{-2}
3DOM Cu_1Fe_1	88.6	0.393	17.7	2.37	2.7×10^{-2}
3DOM Cu_2Fe_1	86.2	0.483	22.4	5.65	6.6×10^{-2}
3DOM Cu_3Fe_1	74.3	0.450	24.2	3.52	4.7×10^{-2}
3DOM Fe	139.2	0.557	16.0	0.11	7.9×10^{-4}
3DOM PM-Cu_2Fe_1 [b]	49.4	0.202	12.9	0.10	2.0×10^{-3}

[a] The reduction conditions: 300°C, 10 psig, H_2/CO =1.0, GHSV = 2000 h^{-1}, and time-on-stream of 48 h. [b] The physical mixture (PM) of 3DOM Cu and 3DOM Fe catalyst, denoted as 3DOM PM-Cu_2Fe_1. [c] BET specific surface areas evaluated in P/P_0 from 0.05 to 0.99, $\pm 2.0\ (m^2 g^{-1})$. [d] Total pore volumes estimated based on the volume adsorbed at P/P_0 of 0.989, $\pm 0.005\ (cm^2 g^{-1})$. [e] Pore sizes derived from the adsorption branches of the isotherms by using the BJH method, ± 0.5 nm. [f] Intrinsic activity is defined as $r_{C_{2+}OH}/S_{BET}$, where $r_{C_{2+}OH}$ is the formation rate of $C_{2+}OH$, S_{BET} is the BET surface area of the reduced catalyst.

Table S5. The Mössbauer fitted parameters of the reduced 3DOM catalysts measured at 27°C. (The reduction conditions: 300°C, 10 psig, H_2/CO =1.0, GHSV = 2000 h^{-1}, and time-on-stream of 48 h). Experimental uncertainties: Isomer shift: IS±0.01mm s^{-1}; Quadrupole splitting: QS±0.01mm s^{-1}; Hyperfine field: ±0.1T; Spectra contribution: ±3.0%. (Note: super-paramagnetic (spm)).

Sample	IS (mm s^{-1})	QS (mm s^{-1})	Hyperfine field (T)	Phase	Spectra contribution (%)
3DOM Fe	0.25	0.09	22.0	χ-Fe_5C_2(II)	32.9
	0.15	0.10	18.8	χ-Fe_5C_2(I)	24.1
	0.23	0.08	10.9	χ-Fe_5C_2(III)	24.1
	0.33	1.06		Fe^{3+} (spm)	18.9
3DOM Cu_1Fe_2	0.26	0.08	22.2	χ-Fe_5C_2(II)	29.3
	0.15	0.12	18.7	χ-Fe_5C_2(I)	24.5
	0.22	0.10	10.6	χ-Fe_5C_2(III)	25.8
	0.31	1.06		Fe^{3+} (spm)	20.4
3DOM Cu_1Fe_1	0.27	0.04	22.2	χ-Fe_5C_2(II)	29.5
	0.16	0.12	18.5	χ-Fe_5C_2(I)	24.3
	0.23	0.11	10.7	χ-Fe_5C_2(III)	25.5
	0.31	1.06		Fe^{3+} (spm)	20.7
3DOM Cu_2Fe_1	0.26	0.05	22.1	χ-Fe_5C_2(II)	27.0
	0.20	0.05	18.1	χ-Fe_5C_2(I)	31.1
	0.21	0.07	10.5	χ-Fe_5C_2(III)	20.4
	0.32	1.07		Fe^{3+} (spm)	21.5
3DOM Cu_3Fe_1	0.28	0.04	22.0	χ-Fe_5C_2(II)	26.2
	0.15	0.11	18.1	χ-Fe_5C_2(I)	24.9
	0.22	0.12	10.5	χ-Fe_5C_2(III)	24.5
	0.31	1.07		Fe^{3+} (spm)	24.4

Table S6. Coordination environment (coordination numbers, bond lengths and their mean squared disorder values) of Cu and Fe atoms of 3DOM Cu_2Fe_1 catalyst under *in situ* CO+H_2 (H_2/CO = 1) reduction in different temperatures. All results correspond to the room temperature at which EXAFS data were collected. The last column contains the best fit values of the photoelectron energy origin correction.

3DOM Cu_2Fe_1 catalyst	CO+H_2	Scatter	N×S_0^2	R (Å)	σ^2(Å^2)	ΔE (eV)
Cu K-edge	RT	Cu–O	1.72±1.09	1.942±0.042	0.0015±0.0033	7.4±1.8
		Cu–Cu	3.44±2.18	2.849±0.054	0.0074±0.0094	7.4±1.8
	50 ℃	Cu–O	0.97±0.24	1.896±0.036	0.0056±0.0059	2.8±0.5
		Cu–Cu	1.95±0.49	2.963±0.148	0.0032±0.0184	2.8±0.5
	100 ℃	Cu–O	0.98±0.27	1.890±0.043	0.0056±0.0064	2.2±0.7
		Cu–Cu	1.96±0.55	2.918±0.640	0.0029±0.0573	2.2±0.7
	150 ℃	Cu–O	1.01±0.94	1.908±0.152	0.0055±0.0229	3.5±0.2
		Cu–Cu	2.01±1.88	2.933±0.439	0.0030±0.0283	3.5±0.2
	200 ℃	Cu–O	1.88±1.71	1.948±0.028	0.0014±0.0069	–0.6±0.1
		Cu–Cu	3.75±3.42	2.854±0.112	0.0081±0.0265	–0.6±0.1
	250 ℃	Cu–Cu	8.88±4.21	2.563±0.031	0.0079±0.0034	–1.8±0.1
	300 ℃	Cu–Cu	7.48±1.10	2.543±0.008	0.0094±0.0013	3.8±1.2
	350 ℃	Cu–Cu	6.47±4.38	2.570±0.026	0.0076±0.0048	10.3±1.0
	400 ℃	Cu–Cu	6.86±4.87	2.568±0.024	0.0080±0.0054	9.6±1.4
Fe K-edge	RT	Fe_{oct}–O	3.10±0.38	1.932±0.011	0.0081±0.0017	–7.8±1.4
		Fe_{tet}–Fe_{tet}	9.30±1.13	3.319±0.011	0.0054±0.0011	–7.8±1.4
	50 ℃	Fe_{oct}–O	3.23±1.30	1.928±0.021	0.0094±0.0042	–7.9±0.6
		Fe_{tet}–Fe_{tet}	9.68±3.90	3.310±0.023	0.0023±0.0043	–7.9±0.6
	100 ℃	Fe_{oct}–O	2.59±0.79	1.923±0.015	0.0062±0.0026	–8.4±1.1
		Fe_{tet}–Fe_{tet}	7.76±2.36	3.300±0.017	0.0003±0.0027	–8.4±1.1
	150 ℃	Fe_{oct}–O	2.67±0.75	1.928±0.015	0.0070±0.0026	–8.0±0.8
		Fe_{tet}–Fe_{tet}	8.00±2.25	3.304±0.015	0.0006±0.0025	–8.0±0.8
	200 ℃	Fe_{oct}–O	2.34±0.74	1.910±0.016	0.0045±0.0025	–13.6±1.2
		Fe_{tet}–Fe_{tet}	7.01±2.23	3.272±0.019	0.0007±0.0029	–13.6±1.2
	250 ℃	Fe_{oct}–O	2.83±0.84	1.935±0.017	0.0081±0.0029	–7.1±0.5
		Fe_{tet}–Fe_{tet}	8.50±2.53	3.321±0.021	0.0021±0.0034	–7.1±0.5
	300 ℃	Fe–C	4.41±0.96	1.645±0.054	0.0458±0.0113	–3.1±0.8
		Fe–Fe	4.41±0.96	2.578±0.041	0.0137±0.0024	–3.1±0.8
	350 ℃	Fe–C	5.61±1.43	1.679±0.032	0.0514±0.0054	–0.7±0.2
		Fe–Fe	5.61±1.43	2.611±0.019	0.0140±0.0020	–0.7±0.2
	400 ℃	Fe–C	5.54±1.70	1.738±0.047	0.0287±0.0082	–8.2±1.0
		Fe–Fe	5.54±1.70	2.577±0.020	0.0159±0.0024	–8.2±1.0

Note: Cu K-edge (RT to 200℃): Δk=2.0–11.0 Å^{-1} and ΔR=1.0–4.0 Å; Cu K-edge (250 to 400℃): Δk=2.5–12.0 Å^{-1} and ΔR=1.7–5.1 Å; Fe K-edge (RT to 250℃): Δk=3.4–12.6 Å^{-1} and ΔR=1.0–4.0 Å; Fe K-edge (300 to 400℃): Δk=2.8–12.1 Å^{-1} and ΔR=1.0–3.0 Å. ΔN=±10%. N: coordination number; S_0^2: amplitude reduction factor; R: bonding distance; σ^2: Debey-Waller factor; ΔE: edge energy shift. Reference data: Cu–O and Cu–Cu bond distance in CuO = 1.951 and 2.901 Å, respectively. Cu–Cu bond distance in Cu metal = 2.553 Å. Fe_{oct}–O and Fe_{tet}–Fe_{tet} bond distance in Fe_3O_4 = 1.935 and 3.482 Å, respectively. Fe–C and Fe–Fe bond distance in χ-Fe_5C_2 = 1.696 and 2.520 Å, respectively.

Table S7. The adsorption energy (E_{ads}/kJ·mol^{-1}) and key geometrical parameters (Å) of reactants, products, and possible intermediates species involved in CO hydrogenation to the formation of C_2-hydrocarbons and C_2-oxygenates on χ-Fe_5C_2(510) surface.

Species	E_{ads}	Configuration	$d_{Fe–C}$	$d_{Fe–O}$	$d_{Fe–H}$
C	707.3	4F2	1.839, 1.863, 1.901, 1.926		
H	292.5	3F8			1.751, 1.768, 1.806
O	652.5	3F7		1.868, 1.878, 1.908	
OH	410.8	3F7		1.987, 2.041,2.050	
CO	190.5	4F2	1.971, 2.000		
CH	706.0	4F2	1.928, 1.971, 2.038, 2.062		
CH_2	447.5	4F2	1.941, 2.069, 2.073, 2.221		1.716
CH_3	233.2	3F7	2.130, 2.183, 2.211		
CHO	294.3	4F2	1.977, 1.979	1.919, 2.039	
CH_2O	166.1	4F2	2.233, 2.274	2.229, 2.292	1.863
CH_3O	310.1	2F2		1.919, 1.940	
COH	354.1	4F2	1.945, 1.983, 2.076, 2.105		
CHOH	301.1	1F3	1.821		
CH_2OH	200.2	3F7	2.030, 2.250	2.136	
CH_3OH	65.8	1F3		2.070	
CHCO	349.1	4F2	1.944, 2.014, 2.100, 2.208, 2.242		
CH_2CO	291.5	4F2	1.960, 2.032, 2.103	1.957	
CH_3CO	198.2	4F2	1.999, 2.006	1.914, 2.041	
CHCHO	443.7	4F2	1.973, 1.975, 2.036, 2.320	1.879	
CH_2CHO	253.1	4F2	2.050, 2.108, 2.313	1.887	
CH_3CHO	63.1	2F2		2.007, 2.099	
CH_4	1.6		2.533		
C_2H_2	266.5	2F1	1.933, 1.969, 1.989, 2.123, 2.136		
C_2H_4	102.6	4F2	2.023, 2.083, 2.281, 2.320		
C_2H_6	2.9		2.756, 3.760		

Table S8. The possible elementary reactions involved in CO hydrogenation to the formation of C_2-hydrocarbons and C_2-oxygenates together with the activation barrier (E_a) and reaction energy (ΔH) on χ-Fe_5C_2(510) surface.

	Elementary reactions	Transition states	E_a(kJ·mol^{-1})	ΔH(kJ·mol^{-1})
R1.1	CO→C+O	TS1.1	128.7	–35.9
R1.2	CO+H→CHO	TS1.2	121.4	84.4
R1.3	CO+H→COH	TS1.3	188.2	83.8
R1.4	C+H→CH	TS1.4	106.1	35.7
R1.5	CHO→CH+O	TS1.5	61.0	–68.8
R1.6	CHO+H→CH+OH	TS1.6	84.6	–17.3
R1.7	CHO+H→CHOH	TS1.7	167.2	125.8
R1.8	CHOH→CH+OH	TS1.8	20.0	–143.1
R1.9	CHOH+H→CH+H_2O	TS1.9	153.9	–81.2
R1.10	CHO+H→CH_2O	TS1.10	51.1	19.3
R1.11	CH+H→CH_2	TS1.11	109.0	83.4
R1.12	CHO+H→CH_2+O	TS1.12	77.2	–10.3
R1.13	CH_2O→CH_2+O	TS1.13	75.3	–29.6
R1.14	CH_2O+H→CH_2+OH	TS1.14	29.9	20.8
R1.15	CH_2O+H→CH_2OH	TS1.15	172.9	109.3
R1.16	CH_2OH→CH_2+OH	TS1.16	29.4	–88.5
R1.17	CH_2O+H→CH_3O	TS1.17	64.8	15.6
R1.18	CH_2+H→CH_3	TS1.18	44.7	5.6
R1.19	CH_2O+H→CH_3+O	TS1.19	63.7	–64.6
R1.20	CH_3O→CH_3+O	TS1.20	139.1	–80.2
R1.21	CH_3O+H→CH_3+OH	TS1.21	79.0	–29.7
R1.22	CH_3O+H→CH_3OH	TS1.22	128.9	74.9
R1.23	CH→C+H	TS1.23	70.4	–35.7
R1.24	CH+CH→C_2H_2	TS1.24	35.9	–1.0
R1.25	CH+CO→CHCO	TS1.25	144.5	120.5
R1.26	CH+CHO→CHCHO	TS1.26	82.4	64.6
R1.27	CH_2→CH+H	TS1.27	25.6	–83.4
R1.28	CH_2+CH_2→C_2H_4	TS1.28	48.2	–31.9
R1.29	CH_2+CO→CH_2CO	TS1.29	113.3	61.7
R1.30	CH_2+CHO→CH_2CHO	TS1.30	71.2	–35.2
R1.31	CH_3→CH_2+H	TS1.31	39.0	–5.6
R1.32	CH_3+H→CH_4	TS1.32	79.4	32.4
R1.33	CH_3+CH_3→C_2H_6	TS1.33	162.5	–3.0
R1.34	CH_3+CO→CH_3CO	TS1.34	137.3	24.2
R1.35	CH_3+CHO→CH_3CHO	TS1.35	132.1	59.7

Table S9. Calculated adsorption energies and geometric information for CO insertion into CH_x (x = 1–3) to C_2-oxygenates on Cu^0–χ-Fe_5C_2(510) and χ-Fe_5C_2(510) surfaces, in comparison to that on Rh(111) surface reported by Zhao *et al*.[21] E_H, E_{CO}, E_{CH}, E_{CH_2} and E_{CH_3} stand for the adsorption energies of H, CO, CH, CH_2 and CH_3, respectively. E_a is the activation barrier of CO insertion into CH_x (x = 1–3) reaction. d_{TS} is the distance between two C atoms in the transition states for CO insertion reactions. The corresponding geometry structures on Cu^0–χ-Fe_5C_2(510) and χ-Fe_5C_2(510) are shown in **Figure S23**.

Parameters	Cu^0–χ-Fe_5C_2(510)	χ-Fe_5C_2(510)	Rh(111)[21]
E_H (kJ·mol^{-1})	289.5	292.5	273.1
E_{CO} (kJ·mol^{-1})	196.8	190.5	194.9
E_{CH} (kJ·mol^{-1})	658.2	706.0	660.0
E_{CH_2} (kJ·mol^{-1})	423.2	447.5	413.0
E_{CH_3} (kJ·mol^{-1})	204.0	233.2	188.2
E_a(CO+CH→CHCO)	64.8	144.5	129.3
d_{TS} (Å)	1.742	1.531	1.650
E_a(CO+CH_2→CH_2CO)	32.5	113.3	120.6
d_{TS} (Å)	1.824	1.520	1.790
E_a(CO+CH_3→CH_3CO)	114.4	137.3	149.6
d_{TS} (Å)	1.767	1.959	1.860

Table S10. The possible elementary reactions involved in the reactions related to CH_x (x = 1–3) species and ethanol formations together with the activation barrier (E_a) and reaction energy (ΔH) on Cu^0–χ-Fe_5C_2(510) surface.

Elementary reactions		Transition states	E_a (kJ·mol^{-1})	ΔH (kJ·mol^{-1})
R2.1	$CH+CH \rightarrow C_2H_2$	TS2.1	20.1	–96.1
R2.2	$CH+H \rightarrow CH_2$	TS2.2	33.0	–0.2
R2.3	$CH+CO \rightarrow CHCO$	TS2.3	64.8	9.4
R2.4	$CH \rightarrow C+H$	TS2.4	135.4	86.9
R2.5	$CH_2+CH_2 \rightarrow C_2H_4$	TS2.5	14.0	–97.9
R2.6	$CH_2+CO \rightarrow CH_2CO$	TS2.6	32.5	7.8
R2.7	$CH_2 \rightarrow CH+H$	TS2.7	33.2	0.2
R2.8	$CH_2+H \rightarrow CH_3$	TS2.8	36.8	–33.0
R2.9	$CH+CH_2 \rightarrow CHCH_2$	TS2.9	45.3	–56.6
R2.10	$CH_3 \rightarrow CH_2+H$	TS2.10	69.7	33.0
R2.11	$CH_3+H \rightarrow CH_4$	TS2.11	79.9	–23.3
R2.12	$CH_3+CO \rightarrow CH_3CO$	TS2.12	114.4	31.5
R2.13	$CH_3+CH_3 \rightarrow C_2H_6$	TS2.13	131.0	–90.1
R2.14	$CHCO+H \rightarrow CH_2CO$	TS2.14(**TS1**)	37.5	24.1
R2.15	$CHCO+H \rightarrow CHCHO$	TS2.15(**TS2**)	74.6	5.9
R2.16	$CH_2CO+H \rightarrow CH_3CO$	TS2.16(**TS3**)	34.5	–3.1
R2.17	$CH_2CO+H \rightarrow CH_2CHO$	TS2.17(**TS4**)	92.9	–66.1
R2.18	$CH_2CO+H \rightarrow CH_2COH$	TS2.18(**TS5**)	128.1	76.1
R2.19	$CH_3CO+H \rightarrow CH_3CHO$	TS2.19(**TS6**)	47.1	–14.5
R2.20	$CH_3CO+H \rightarrow CH_3COH$	TS2.20(**TS7**)	140.7	87.8
R2.21	$CH_3CHO+H \rightarrow CH_3CH_2O$	TS2.21(**TS8**)	40.8	–28.4
R2.22	$CH_3CHO+H \rightarrow CH_3CHOH$	TS2.22(**TS9**)	155.8	36.2
R2.23	$CH_3CH_2O+H \rightarrow C_2H_5OH$	TS2.23(**TS10**)	114.2	–11.1

Note: TS2.14(**TS1**) denotes that the transition state TS2.14 in the Supplementary Figures is numbered as the transition state **TS1** in the main text, the same as other transition states hereafter.

Supporting Information Methods.

Synthesis and Reduction of Rh/SiO_2 Catalyst. $Rh(NO_3)_3$ hydrate (CAS#10139-58-9, Molecular Weight of 288.92, Sigma-Aldrich) and silica dioxide (CAS#:112945-52-5, Molecular weight of 60.08, Sigma-Aldrich) was used in silica supported rhodium catalyst preparation. Silica dioxide was first ground and sieved to 30–50 mesh, washed using boiled distilled water for 3 times, and then calcined in air at 500 ℃ for 5 h before being used as a support. The (5wt%)Rh/SiO_2 catalyst was prepared by a wetness impregnation of the calcined silica dioxide (4.75g) with an aqueous solution of $Rh(NO_3)_3$ hydrate (0.70g) for 24 h, followed by drying at 110 ℃ overnight before being calcined in air at 500 ℃ for 5 h. Prior to catalytic reaction, the (5wt%)Rh/SiO_2 catalyst was in situ reduced with syngas (H_2/CO = 1) at atmospheric pressure and 500 ℃ for 5 h.

X-ray diffraction. XRD measurements were carried out by using an Ultima III X-ray diffractometer (Rigaku Americas, The Woodlands, TX) with Cu Kα radiation (λ = 0.154 nm) operated at 40 kV and 44 mA at a rate of 0.08 ° min^{-1}.

X-ray Photoelectron Spectroscopy. XPS was recorded with a PHI 1600 XPS surface Analysis System (Physical Electronics, Eden Prairie, MN). The instrument used a PHI 10-360 spherical capacitor energy analyzer and an Omni Focus II small-area lens to focus the incident source to an 800 µm diameter surface analysis area, using an achromatic Mg Kα X-ray source (hυ = 1253.6 eV) operating at 300 W and 15 kV. Survey spectra were gathered using an average of 10 scans with pass energy of 26.95 eV and running from 1100 to 0 eV. High-resolution spectra were gathered using an average of 15 scans with pass energy of 23.5 eV and a step size of 0.1 eV. The incident sample angle was held constant at 45°. XPS data was collected and averaged using PHI Surface Analysis software, Version 3.0 (Physical Electronics, Eden Prairie, MN). XPS data was analyzed by using Casa XPS software. The C1s peak of adventitious carbon (284.5 eV) was used as a reference for estimating the binding energy. The binding energies were given with an accuracy of ±0.1 eV.

High Resolution Transmission Electron Microscopy. HRTEM images were obtained on a JEOL 2100 electron microscope (JEOL, Japan) operated at 200 kV. The catalyst samples were dispersed in ethanol and sonicated for 20 min and then deposited over a formvar Nickel grid.

The Textural Properties Measurement. The textural properties (BET specific surface areas, pore volume, pore size) of catalysts were measured with linear parts of the BET plot of the N_2 isotherms. Nitrogen adsorption/desorption isotherms at –196 ℃ were recorded using a Micromeritics ASAP 2010 porosimeter. The samples were outgassed in N_2 flow at 250 ℃ for 4 h before the measurement.

Supporting Information References

(1) Lu, Y.; Cao, B.; Yu, F.; Liu, J.; Bao, Z.; Gao, J. *ChemCatChem* **2014**, *6*, 473–478.
(2) Steynberg, P. J.; van de Berg, J. A.; Janse van Rensburg, W. *J. Phys.: Condens. Matter* **2008**, *20*, 064238.
(3) Retief J. J. *Powder Diffr.*, **1999**, *14*, 130−132.
(4) Hofer, L. J. E. & Cohn, E. M. *J. Am. Chem. Soc.*,**1959**, *81*, 1576−1582.
(5) Zhao, S.; Liu, X. -W.; Huo, C. -F.; Li, Y. -W.; Wang, J.; Jiao, H. *J. Catal.*, **2012**, *294*, 47–53.
(6) Pham, T. H., Duan, X., Qian, G., Zhou, X. & Chen, D. *J. Phys. Chem. C* **2014**, *118*, 10170−10176.
(7) Pham, T. H.; Qi, Y.; Yang, J.; Duan, X.; Qian, G.; Zhou, X.; Chen, D.; Yuan, W. *ACS Catal.*, **2015**, *5*, 2203−2208.
(8) Cao, D. -B.; Li, Y. -W.; Wang, J.; Jiao, H. *J. Mol. Catal. A: Chem.*, **2011**, *346*, 55–69.
(9) Huo, C. -F.; Li, Y. -W.; Wang, J.; Jiao, H. *J. Am. Chem. Soc.*, **2009**, *131*, 14713–14721.
(10) Cao, D. -B.; Li, Y. -W.; Wang, J.; Jiao, H. *J. Phys. Chem. C* **2008**, *112*, 14883–14890.
(11) Yang, C.; Zhao, H.; Hou, Y.; Ma, D. *J. Am. Chem. Soc.*, **2012**, *134*, 15814–15821.
(12) Herranz, T.; Rojas, S.; Pérez-Alonso, F. J.; Ojeda, M.; Terreros, P.; Fierro, J. L. G. *J. Catal.*, **2006**, *243*, 199–211.
(13) Olus Ozbek, M.; Niemantsverdriet, J. W. *J. Catal.*, **2014**, *317*, 158–166.
(14) Wang, D.; Chen, B.; Duan, X.; Chen, D.; Zhou, X. *J. Energy Chem.*, **2016**, *25*, 911–916.
(15) Truong, C. M.; Rodriguez, J. A.; Goodman, D. W. *Surf. Sci.*, **1992**, *271*, L385–L391.
(16) Wang, T.; Tian, X. X.; Li, Y. W.; Wang, J. G.; Beller, M.; Jiao, H. J. *ACS Catal.*, **2014**, *4*, 1991−2005.
(17) Mao, W.; Su, J.; Zhang, Z.; Xu, X. -C.; Dai, W.; Fu, D.; Xu, J.; Zhou, X.; Han, Y. -F. *Chem. Eng. Sci.*, **2015**, *135*, 312–322.
(18) Mei, D.; Rousseau, R.; Kathmann, S. M.; Glezakou, V. -A.; Engelhard, M. H.; Jiang, W.; Wang, C.; Gerber, M. A.; White, J. F.; Stevens, D. J. *J. Catal.*, **2010**, *271*, 325–342.
(19) Liu, J.; Tao, R.; Guo, Z.; Regalbuto, J. R.; Marshall, C. L.; Klie, R. F.; Miller, J. T.; Meyer, R. J. *ChemCatChem* **2013**, *5*, 3665–3672.
(20) Yu, J.; Mao, D.; Han, L.; Guo, Q.; Lu, G. *Catal. Commun.*, **2012**, *27*, 1–4.
(21) Zhao, Y. -H.; Sun, K.; Ma, X.; Liu, J.; Sun, D.; Su, H. -Y.; Li, W. -X. *Angew. Chem. Int. Ed.*, **2011**, *50*, 5335–5338.